

UNCLASSIFIED

SRTC-NN-95-25

Revision 1

August 11, 1997

**ALGE: A 3-D THERMAL PLUME PREDICTION
CODE FOR LAKES, RIVERS AND ESTUARIES (U)**

**SPECIAL PROGRAMS
SAVANNAH RIVER TECHNOLOGY CENTER**

**Prepared by:
A. J. Garrett**

**Approved by:
A. L. Boni**

UNCLASSIFIED

UNCLASSIFIED

TABLE OF CONTENTS

	Page
ABSTRACT	4
1.0 INTRODUCTION	5
2.0 MODEL EQUATIONS	5
2.1 Hydrodynamic Equations	5
2.2 Mixing Parameterization	8
2.2.1 Horizontal Eddy Viscosity	8
2.2.2 Vertical Eddy Viscosity	9
2.3 Energy Transfer	10
2.3.1 Sensible and Latent Heat Transfer	10
2.3.2 Shortwave (Solar) Radiation	12
2.3.3 Longwave Radiation	14
2.4 Mass and Energy Sources and Sinks	15
3.0 NUMERICAL METHODS	15
3.1 Finite Differencing	15
3.2 Boundary Conditions	19
3.3 Nudging	19
4.0 INPUTS FOR NUMERICAL SIMULATIONS	21
4.1 Surface Meteorological Data	21
4.2 Upper Air Meteorological Data	21
4.3 Tidal Forcing	22
4.4 Land-Water Distribution	23
4.5 Water Depths	23
4.6 Nudging Inputs	23
4.7 Other Input Parameters	24
5.0 BENCHMARKING AND SAMPLE SIMULATIONS	24
5.1 Delaware Bay	24
5.1.1 Baseline Simulation	24
5.1.2 Sensitivity to Magnitude of Roughness Length	29
5.2 SRS Pond "C" Analysis	30
5.3 SRS "L" Lake	32
5.4 Savannah River	34
5.5 Squaw Creek Reservoir	36
REFERENCES	39
FIGURES	42

UNCLASSIFIED

UNCLASSIFIED

ALGE: A 3-D THERMAL PLUME PREDICTION CODE FOR LAKES, RIVERS AND ESTUARIES

A. J. Garrett

ABSTRACT

ALGE is a 3-D hydrodynamic code which solves the momentum, mass and energy conservation equations to predict the movement and dissipation of thermal plumes discharged into cooling lakes, rivers and estuaries. The cooling lake simulations include recirculation and buoyancy driven flow. The estuarine simulations include prediction of tidal current speeds and directions. ALGE also simulates wind-driven circulations, and can combine wind stress effects with tidal and buoyancy forces. Energy is exchanged with the model atmosphere through turbulent sensible and latent heat transfer, and by shortwave (solar) and longwave (thermal) radiation transfer, including the effects of clouds. The coordinates are Cartesian. The governing PDE's are solved in flux form with simple upwind and centered differencing schemes. ALGE can model highly irregular land-water boundaries and water depth distributions, including islands. ALGE was designed to produce high resolution simulations for node-to-node matching with aircraft or satellite thermal imagery. This report compares ALGE's simulations to cooling pond data from the Savannah River Site and Texas, thermal plume data from the Savannah River, and tidal data from Delaware Bay. The accuracy of ALGE's predictions depends on the quality of available input data (such as water depths and resolution and completeness of thermal images). In general, ALGE's temperature predictions do not appear to be biased high or low and ALGE reproduces observed temperature distribution patterns. Root-mean-square-errors (RMSE's) derived from node-to-node matching over the whole computational domain ranged from about one to three °C.

UNCLASSIFIED

UNCLASSIFIED

ALGE: A 3-D THERMAL PLUME PREDICTION CODE FOR LAKES, RIVERS AND ESTUARIES

A. J. Garrett

1.0 INTRODUCTION

Accurate predictions of the transport and dissipation of thermal discharges into lakes, rivers and estuaries are needed to verify regulatory compliance. In the non-proliferation arena, thermal discharges can be analyzed to generate operating power estimates for nuclear reactors which may be producing weapons materials. Realistic predictions of temperature distributions can only be made with multi-dimensional numerical models that solve the hydrodynamic equations and the energy conservation equation. The alternative is to use statistical correlations based on large amounts of empirical data, which is usually not an option. Verification of numerical predictions of temperature distributions is often limited to a few point measurements. Scattered surface measurements produce an incomplete verification data set. However, when thermal imagery from aircraft or satellites is available, with some surface data for calibration, much more complete assessments of model skill can be performed.

This report describes a 3-D hydrodynamic code (ALGE) that was developed specifically for applications where thermal imagery is available for cell to cell comparisons to code predictions. The following sections of this report describe the governing equations, numerical methods, code structure and test problems and benchmark results.

2.0 MODEL EQUATIONS

2.1 Hydrodynamic Equations

The following set of equations is very similar to those used by most researchers to predict the behavior of bodies of water with free surfaces, e.g., see Blumberg and Mellor (1983), Oey, Mellor and Hires (1985), Froehlich (1989), Jin and Kranenburg (1993), and Johnson, et al (1993). All of these researchers use vertically averaged hydrodynamic equations to predict the water surface level over space and time. Some make a separate 3-D flow prediction using the vertically averaged (2-D) surface level prediction as an upper boundary condition. The vertically averaged model is known as the external mode and the 3-D system which uses the 2-D level predictions as an upper boundary condition is known as the internal mode. Splitting the problem into internal and external mode reduces computing time by eliminating the restrictive speed of a free-surface gravity wave from the stability criteria for the 3-D calculation.

UNCLASSIFIED

UNCLASSIFIED

Most of the modelers listed above use some sort of variable transformation to minimize the number of cells in the model domain. For many 3-D models, some version of the Phillips (1957) sigma coordinate system is used. Some authors found that the sigma system prevented the code from correctly maintaining vertical stratification in deep channels, and they returned to a simple Cartesian system for the vertical coordinate (Johnson et al, 1993). ALGE uses Cartesian coordinates in the horizontal and vertical planes.

The 3-D version of ALGE solves the following standard set of hydrostatic equations:

$$\frac{\partial u}{\partial t} = -\frac{\partial uu}{\partial x} - \frac{\partial uv}{\partial y} - \frac{\partial wu}{\partial z} - \frac{1}{\rho} \frac{\partial p}{\partial x} + fv + \frac{\partial}{\partial x} \left(K_H \frac{\partial u}{\partial x} \right) + \frac{\partial}{\partial y} \left(K_H \frac{\partial u}{\partial y} \right) + \frac{\partial}{\partial z} \left(K_z \frac{\partial u}{\partial z} \right) \quad (1)$$

$$\frac{\partial v}{\partial t} = -\frac{\partial uv}{\partial x} - \frac{\partial vv}{\partial y} - \frac{\partial wv}{\partial z} - \frac{1}{\rho} \frac{\partial p}{\partial y} - fu + \frac{\partial}{\partial x} \left(K_H \frac{\partial v}{\partial x} \right) + \frac{\partial}{\partial y} \left(K_H \frac{\partial v}{\partial y} \right) + \frac{\partial}{\partial z} \left(K_z \frac{\partial v}{\partial z} \right) \quad (2)$$

$$\frac{\partial T}{\partial t} = -\frac{\partial uT}{\partial x} - \frac{\partial vT}{\partial y} - \frac{\partial wT}{\partial z} + \frac{\partial}{\partial x} \left(K_H \frac{\partial T}{\partial x} \right) + \frac{\partial}{\partial y} \left(K_H \frac{\partial T}{\partial y} \right) + \frac{\partial}{\partial z} \left(K_z \frac{\partial T}{\partial z} \right) \quad (3)$$

$$\frac{\partial w}{\partial z} = -\frac{\partial u}{\partial x} - \frac{\partial v}{\partial y} \quad (4)$$

$$\frac{\partial p}{\partial z} = -\rho g \quad (5)$$

In the system (1) through (5), u , v and w are the velocity components, T is temperature, K_H and K_z are the horizontal and vertical diffusion coefficients, f is the Coriolis parameter, g is gravitational acceleration, p is hydrostatic pressure and ρ is density of water. In the surface layer of the model, wind stress and energy source/sink terms are added to (1) through (3) to account for wind stress and atmospheric heat exchange, (see Eqs. (7)-(9) below). A logarithmic relationship (see Eq. 11) is used to model bottom drag at the lower level of the model.

Vertically integrated versions of (1), (2) and (4) are also solved to produce time-varying free surface elevations for use in computation of pressure gradients in (1) and (2) and pressure in (5). The vertically integrated forms of (1), (2) and (4) are derived by first introducing a transformed, terrain following vertical coordinate:

UNCLASSIFIED

$$z^* = z - z_g(x, y) \quad (6)$$

In (6), z_g is the height of the solid material under the water above some arbitrary reference height (z_g can be negative). The transformation defined by (6) was used by Garrett and Smith (1984) in an atmospheric application. It produces equations (7) through (9) below, which are vertically averaged forms of the momentum and mass conservation equations. (Note that the asterisk has been dropped from z^* .)

$$\begin{aligned} \frac{\partial uh}{\partial t} = & -\frac{\partial u^2 h}{\partial x} - \frac{\partial uvh}{\partial y} + h \frac{\partial}{\partial x} \left(K_H \frac{\partial u}{\partial x} \right) + h \frac{\partial}{\partial y} \left(K_H \frac{\partial u}{\partial y} \right) + fvh \\ & - \frac{g}{\rho_o} \left(\frac{h^2}{2} \frac{\partial \rho}{\partial x} + \rho_o h \frac{\partial h}{\partial x} + \rho_o h \frac{\partial z_g}{\partial x} \right) - C_D U u + C_s \rho_a W^2 \cos \psi / \rho_w \end{aligned} \quad (7)$$

$$\begin{aligned} \frac{\partial vh}{\partial t} = & -\frac{\partial uvh}{\partial x} - \frac{\partial v^2 h}{\partial y} + h \frac{\partial}{\partial x} \left(K_H \frac{\partial v}{\partial x} \right) + h \frac{\partial}{\partial y} \left(K_H \frac{\partial v}{\partial y} \right) - fuh \\ & - \frac{g}{\rho_o} \left(\frac{h^2}{2} \frac{\partial \rho}{\partial y} + \rho_o h \frac{\partial h}{\partial y} + \rho_o h \frac{\partial z_g}{\partial y} \right) - C_D U v + C_s \rho_a W^2 \sin \psi / \rho_w \end{aligned} \quad (8)$$

$$\frac{\partial h}{\partial t} = -\frac{\partial uh}{\partial x} - \frac{\partial vh}{\partial y} + M_s \quad (9)$$

where u and v are the horizontal velocity components and h is water depth. Also,

$$U = (u^2 + v^2)^{\frac{1}{2}} \quad (10)$$

and K_H is the horizontal eddy diffusion coefficient, f is the Coriolis parameter, g is gravitational acceleration, ρ is water density, ρ_o is the reference density (1 gm/cm³), C_D is the bottom drag coefficient, C_s is the air-water surface drag coefficient, ρ_a is air density, W is wind speed, ψ is the angle of the x-axis from north, and M_s is mass source. The drag coefficient is related to the roughness length by the logarithmic law:

$$C_d = k^2 [\ln(z_1 / z_o)]^2 \quad (11)$$

UNCLASSIFIED

UNCLASSIFIED

where k is von Karman's constant (0.4) and z_1 is the first node above the bottom. The roughness length is user specified.

A complete derivation of (7)-(9) is given in Garrett (1993).

2.2 Mixing Parameterizations

2.2.1 Horizontal Eddy Viscosity

The horizontal eddy viscosities and diffusivities (K_H) have three components:

$$K_H = K_f + K_s + K_b \quad (12)$$

The three components refer to turbulent mixing caused by bottom roughness, horizontal velocity shear and buoyancy forces, respectively. The component that represents the effects of bottom roughness is drawn from Froehlich (1989):

$$K_f = 0.6u_*h + K_o \quad (13)$$

The standard logarithmic law is used to evaluate the friction velocity (u_*), and the constant (K_o) is set equal to 0.1 (m^{**2}/s). [Since this term is not dependent on mesh size, it is important only in simulations where velocities are high and horizontal mesh size is small, e.g., river simulations.]

The second component is based on a version of the Smagorinsky (1963) model, as described by Galperin and Orszag (1993):

$$K_s = C_{sh}\Delta^2 S \quad (14)$$

$$\text{where } C_{sh} = 0.02, \Delta = (\Delta x \Delta y)^{0.5} \quad (15)$$

and

$$S = (S_{ij}S_{ij})^{\frac{1}{2}} \quad (16)$$

S is a scalar function of the large scale strain rate tensor, i.e.,

$$S_{ij} = \frac{1}{2} \left(\frac{\partial u_i}{\partial x_j} + \frac{\partial u_j}{\partial x_i} \right) \quad (17)$$

For quasi-horizontal environmental flows S reduces to:

UNCLASSIFIED

UNCLASSIFIED

$$S = \left[\frac{1}{2} \left(\frac{\partial u}{\partial y} + \frac{\partial v}{\partial x} \right)^2 \right]^{\frac{1}{2}} \quad (18)$$

The third component adds the effects of density gradients on the sub-grid scale spread of thermal plumes by defining a velocity scale based on a balance between buoyancy and frictional drag:

$$K_b = V_b \Delta_{xy} C_b \quad (19)$$

where

$$V_b = \left[u_b^2 + v_b^2 \right]^{\frac{1}{2}} \quad (20)$$

with

$$u_b = \sqrt{\frac{gh^2}{C_D \rho_o} \left| \frac{\partial \rho}{\partial x} \right|}, v_b = \sqrt{\frac{gh^2}{C_D \rho_o} \left| \frac{\partial \rho}{\partial y} \right|} \quad (21)$$

$$\Delta_{xy} = \sqrt{\Delta x \Delta y} \quad (22)$$

and $C_b = 0.03$ (estimated).

★ This component is important when velocities are low and buoyancy forces are responsible for much of the movement of the water.

2.2.2 Vertical Eddy Viscosity

ALGE currently uses a simple first-order scheme to compute vertical eddy viscosity that combines functional forms from Jin and Kranenburg (1993) and Pacanowski and Philander (1981):

$$K_z = k u_* z (1 - z/h) / (1 + \alpha R_z)^n \quad (23)$$

where u_* is the maximum of the bottom and surface (wind) friction velocities, i.e.,

$$u_* = \max(|u_b|, |u_s|) \quad (24)$$

UNCLASSIFIED

UNCLASSIFIED

and z is the vertical coordinate, h is total depth, α is a constant with a value of 5, R_i is the layer Richardson number and n is a constant with a value of 2. The surface friction velocity $|u_s^*|$ is defined to be $0.001W$, where W is the wind speed in m/s (Hicks, 1972). The bottom friction velocity $|u_b^*|$ is computed from the standard logarithmic relationship. The vertical eddy viscosity and vertical eddy diffusivity are assumed to be equal.

Finally, when a simulated physical process (such as cooling at the surface caused by heat loss to the atmosphere) has led to an absolutely unstable temperature lapse rate at a (x,y) location, ALGE averages the temperatures in the two cells that are unstably stratified. This averaging is repeated throughout the vertical column wherever there is an unstable stratification. This process simulates the rapid overturning of unstably stratified columns of water, and is similar to the approach used by Johnson et al (1993) to solve the same problem. Note that only temperature and not momentum are averaged when two vertical cells are unstable.

2.3 Energy Transfer

Exchange of energy between the surface layer of a body of water modeled by ALGE and the atmosphere is computed separately from the advection and diffusion computations in (3) above (time-splitting):

$$\frac{dT}{dt} = (H_s + H_L + S_w + L_w) / (\Delta Z_s \rho_w c_{pw}) \quad (25)$$

where H_s is sensible heat flux, H_L is latent heat flux, S_w is solar radiation, L_w is thermal radiation, ΔZ_s is surface layer depth, ρ_w is water density and c_{pw} is specific heat of water.

A simple iterative Euler method is used to solve (25), because the time steps imposed by the CFL limit (Section 3.0) are extremely short relative to the time scale required for significant temperature change. The solution to (25) is carried out in a separate subroutine which is called at a frequency that can be specified by the user.

2.3.1 Sensible and Latent Heat Transfer

The sensible (H_s) and latent (H_L) heat fluxes are computed according to the relationships developed by Louis (1979). Louis' method makes use of a bulk Richardson number (R_i) for the atmospheric surface layer.

UNCLASSIFIED

UNCLASSIFIED

$$R_i = \frac{gz\Delta\theta}{\theta_m W^2} \quad (26)$$

where:

g = gravitational acceleration,

$\Delta\theta$ = potential temperature difference across surface layer (nominally 30 m)

θ_m = mean potential temperature in surface layer

W = wind speed (m/s)

The fluxes can be written as:

$$H_s = a^2 W \Delta\theta F \rho_a C_p \quad (27)$$

and

$$H_L = a^2 W \Delta q F \rho_a L \quad (28)$$

where:

$R_i = 0.74$

ρ_a = air density

C_p = specific heat of air

L = latent heat of evaporation

F = flux profile parameterization using R_i

Δq = specific humidity difference across surface layer, and

$$a^2 = k^2 / \left[\ln(z/z_o) \right]^2 \quad (29)$$

where:

k = von Karman's constant (0.4)

z_o = roughness length over water (0.0002 m)

The flux profile parameterization F is defined by

$$F = 1 - \frac{bR_i}{1 + C\sqrt{|R_i|}} \quad (30)$$

for $R_i < 0$, and

$$F = (1 + bR_i/2)^{-2} \quad (31)$$

UNCLASSIFIED

UNCLASSIFIED

for $R_i > 0$, and where

$b = 9.4$, and

$$C = 5.3a^2b\sqrt{z/z_o} \quad (32)$$

2.3.2 Shortwave (Solar) Radiation

The model for computing global solar radiation was developed and tested by Garrett (1978, 1980, 1982). In this application, all solar radiation is assumed to be absorbed in the uppermost layer of the simulated body of water. Direct plus diffuse solar radiation reaching the ground is computed from:

$$F = S_o (\tau_d \tau_{ws}^w \tau_{wa}^w)^M \cos \zeta \quad (33)$$

In (33), τ_d , τ_{ws}^w , τ_{wa}^w are transmission functions which parameterize the effects of dry air scattering, water vapor scattering and water vapor absorption, respectively. The exponent w is total atmospheric water vapor content expressed as an equivalent water depth (cm), and M is a pressure-adjusted optical depth. The coefficient S_o is the normal solar flux above the troposphere, and ζ is the zenith angle.

The pressure-adjusted optical depth M is defined by $M = mp/P_o$, where m is the optical depth, p is atmospheric pressure at the location of interest and P_o is sea level pressure (1013 mb). The optical depth is defined by $m = \sec \zeta$ for $\zeta < 70^\circ$, and by

$$m = \left[-R \cos \zeta + (R^2 \cos^2 \zeta + 2RH_s + H_s^2)^{0.5} \right] / H_s \quad (34)$$

for $\zeta > 70^\circ$. Also, R is the radius of the earth (6370 km) and H_s is an atmospheric scale height (10 km).

The transmission functions and S_o are defined by

$$\tau_d = 0.9 + 0.01(-0.1m^2 + 1.3m - 0.6) \quad (35)$$

$$\tau_{ws} = 0.975 \quad (36)$$

$$\tau_{wa} = 1 - \frac{0.19685}{[1 + 1/(0.6992\sqrt{mw})]} \quad (37)$$

UNCLASSIFIED

UNCLASSIFIED

$$S_o = 0.98 S_c (\phi_m / \phi)^2 \quad (38)$$

In (32), 0.98 is a coefficient accounting for absorption by ozone in the stratosphere, S_c is the solar constant (1.94 cal/cm²/s), ϕ_m is the mean earth to sun distance of 1.49X10⁸ km, and ϕ is the actual distance, which is a function of the Julian day (J):

$$\phi = 149 - 2.6 \sin(\pi / 2 - J\pi / 182.5) \quad (39)$$

When clouds are present, transmission functions must be used to deplete the solar flux. Cumulus and stratocumulus are usually the dominant depleters of solar radiation. Transmission functions for these cloud types are:

$$\begin{aligned} \tau_{cu} &= 0.17 - 0.21 \cos \zeta \\ \tau_{st} &= 0.28 - 0.16 \cos \zeta \end{aligned} \quad (40)$$

for $\cos \zeta < 0.2$, and

$$\begin{aligned} \tau_{cu} &= 0.10 + 0.14 \cos \zeta \\ \tau_{st} &= 0.19 + 0.28 \cos \zeta \end{aligned} \quad (41)$$

for $\cos \zeta > 0.2$. The net surface global radiation is:

$$S_w = (1 - A)(1 - \sigma_c + \sigma_c \tau) F \quad (42)$$

where A is albedo of water, σ_c is the amount of cloud cover ($0 < \sigma_c < 1$), and τ is the cloud transmission function. The albedo (A) is computed from relationships in Kondratyev (1969).

$$A = 0.5 \left[\frac{\sin^2(i-r)}{\sin^2(i+r)} + \frac{\tan^2(i-r) \cos^2(i+r)}{\sin^2(i+r)} \right] \quad (43)$$

where r is the angle of refraction and i is the angle of incidence, which are related through n, the refractive index (n=1.33):

$$\sin(r) = \sin(i) / n \quad (44)$$

UNCLASSIFIED

UNCLASSIFIED

2.3.3 Longwave Radiation

The net surface longwave radiative flux is computed with a simplified transmission model that treats emission and absorption in combined spectral bands. The model was developed by Kondratyev (1969) and tested by Garrett (1977). Clouds are treated as blackbodies and emission and absorption above the tropopause is neglected. The general case of partly cloudy skies is treated. The flux contributed by a spectral group j is computed from:

$$L_{wj} = \sigma_{sb} (T_s^4 - T_1^4) + p_j \sum_{i=1}^{I_c} \frac{\phi_i}{k_j} (e^{-k_j w_{i+1}} - e^{-k_j w_i}) + (1 - \sigma_c) \left[p_j \sum_{i=I_c+1}^{I_r} \phi_i (e^{-k_j w_{i+1}} - e^{-k_j w_i}) / k_j \right] + p_j e^{-k_j w_{I_r}} B(T_1)$$

$$L = \int_0^s dL = \int_0^s \sigma_{sb} T^4 - \sigma_{sb} T_1^4$$

$$L = \sigma_{sb} T_s^4 - \sigma_{sb} T_1^4$$

(45)

where

$$\phi_i = \frac{B(w_{i+1}) - B(w_i)}{w_{i+1} - w_i}$$

and

(46)

$$L_w = \sum_{j=1}^J L_{wj}$$

(47)

The variables for the longwave radiation equations are defined below:

- σ_{sb} = Stefan-Boltzmann constant
- T_s = water surface temperature (K)
- T_1 = surface layer air temperature (typically 10 m)
- p_j = weighting coefficient
- k_j = absorption coefficient
- w = atmospheric equivalent water depth (cm)
- σ_c = cloud cover
- B = blackbody flux
- i = computational level
- I_c = cloud level (km)
- I_T = tropopause level

UNCLASSIFIED

UNCLASSIFIED

The absorption and weighting coefficients are:

$$p_1 = 0.25$$

$$p_2 = 0.1$$

$$k_1 = 0.166$$

$$k_2 = 0.8$$

2.4 Mass and Energy Sources and Sinks

Mass (water) can be added to any cell in the water part of the domain. The mass flow rate in cubic meters per second is a code input. If the user specifies multiple cells as mass sources, the total flow rate is divided evenly among these cells. The user can also specify the locations of cells that are mass sinks. The level of the mass sources is also specified. Mass sinks are always assumed to be at the lowest level at a given (x, y) location. Since this is a hydrostatic code, a mass sink is modeled by reducing the water surface elevation at a given location (x,y) at a rate determined by the user-specified input. The corresponding vertical velocity is imposed as a boundary condition at the bottom, with vertical velocities at the bottom computed from Eq. (4). Mass sources are modeled by increasing the water surface elevation at a rate that is determined by the user.

Energy is added to the model domain by specifying the temperature of the mass source, or the user can prescribe a temperature increase from mass intake to mass outflow. If the mass source is subsurface, the temperature in the volume at that level is changed at a rate consistent with the mass supply rate. The vertical velocity in this case has a lower boundary condition of zero, and the 3-D velocity field generated by the mass source will result in mass transport out of the cell(s) with mass source(s).

3.0 NUMERICAL METHODS

3.1 Finite Differencing

The advective terms in the systems (1)-(3) and (7)-(9) are solved by the conservative and transportive upwind differencing scheme described by Roache (1972). This simple differencing scheme is straightforward to implement for a high resolution model with irregular domain boundaries. The diffusion terms are also approximated by a conservative differencing scheme described by Roache (1972). Eqs. (1)-(5) were transformed directly into finite difference equations, whereas Eqs. (7)-(9) were first rewritten using the following definitions (see Jin and Kranenburg 1993):

UNCLASSIFIED

UNCLASSIFIED

$$\begin{aligned} Q_x &= uh \\ Q_y &= vh \end{aligned} \quad (48)$$

Equations (7) through (9) take the following form:

$$\begin{aligned} \frac{\partial Q_x}{\partial t} &= -\frac{\partial Q_x^2 / h}{\partial x} - \frac{\partial Q_x Q_y / h}{\partial y} + h \frac{\partial}{\partial x} \left(K_H \frac{\partial Q_x / h}{\partial x} \right) + h \frac{\partial}{\partial y} \left(K_H \frac{\partial Q_x / h}{\partial y} \right) \\ &+ C_a \rho_a W^2 \cos \psi / \rho_w - C_D U Q_x / h + f Q_y \\ &- \frac{g}{\rho_o} \left[\frac{h^2}{2} \frac{\partial \rho}{\partial x} + \rho_o h \frac{\partial h}{\partial x} + \rho_o h \frac{\partial z_s}{\partial x} \right] \end{aligned} \quad (49)$$

$$\begin{aligned} \frac{\partial Q_y}{\partial t} &= -\frac{\partial Q_x Q_y / h}{\partial x} - \frac{\partial Q_y^2 / h}{\partial y} + h \frac{\partial}{\partial x} \left(K_H \frac{\partial Q_y / h}{\partial x} \right) + h \frac{\partial}{\partial y} \left(K_H \frac{\partial Q_y / h}{\partial y} \right) \\ &+ C_a \rho_a W^2 \sin \psi / \rho_w - C_D U Q_y / h - f Q_x \\ &- \frac{g}{\rho_o} \left[\frac{h^2}{2} \frac{\partial \rho}{\partial y} + \rho_o h \frac{\partial h}{\partial y} + \rho_o h \frac{\partial z_s}{\partial y} \right] \end{aligned} \quad (50)$$

$$\frac{\partial h}{\partial t} = -\frac{\partial Q_x}{\partial x} - \frac{\partial Q_y}{\partial y} + M_s \quad (51)$$

Q_x and Q_y are solved for first and then h . The updated values of h are used to compute u and v from the updated Q values.

Within the model domain, cells that represent land are differentiated from cells that represent water through the use of a two dimensional integer array $ID(x,y)$ that contains 1's for water and 0's for land. Velocity components over land are always zero, and those values are used as boundary conditions for the difference equations for u and v . Since Q_x and Q_y are solved for instead of u and v , h must have a small positive value over land (0.01 m). If this is not done, then the differencing for u and v will result in divisions by zero.

The method described in Roache (1972) is illustrated with a one dimensional form of the advection equation:

$$\frac{\partial Q_x}{\partial t} = -\frac{\partial Q_x Q_x / h}{\partial x} \quad (52)$$

UNCLASSIFIED

In finite difference form:

$$\frac{\Delta Q_i}{\Delta t} = -\frac{(u_r Q_r - u_l Q_l)}{\Delta x} \quad (53)$$

Where:

$$u_r = 0.5 * (Q_{i+1} / h_{i+1} + Q_i / h_i) \quad (54a)$$

$$u_l = 0.5 * (Q_i / h_i + Q_{i-1} / h_{i-1}) \quad (54b)$$

and $Q_r = Q_i$ for $u_r > 0$, $Q_r = Q_{i+1}$ for $Q_r < 0$, and $Q_l = Q_{i-1}$ for $u_l > 0$, $Q_l = Q_i$ for $u_l < 0$. To force conservation (of momentum in this case) algebraically, $u_r = 0$ if the $i+1$ node is land, and $u_l = 0$ if the $i-1$ node is land. Centered differences are used for solution of the mass conservation equations (4) and (51) instead of upwind differences. Pressure gradients in the momentum equations are also approximated by centered differences, which allows upstream wave propagation. The differencing method described above for forcing conservation of momentum is also used to force conservation of energy and mass.

An explicit, conservative method is also used for the differencing of all horizontal diffusion terms (also from Roache 1972, p. 256).

$$\frac{\partial}{\partial x} \left(K_H \frac{\partial \phi}{\partial x} \right) = (K_{i+1/2} (\phi_{i+1} - \phi_i) - K_{i-1/2} (\phi_i - \phi_{i-1})) / \Delta x^2 \quad (55)$$

where

$$K_{i+1/2} = 0.5 * (K_{i+1} + K_i) \quad (56a)$$

and

$$K_{i-1/2} = 0.5 * (K_i + K_{i-1}) \quad (56b)$$

and

$$\phi = Q_x / h, Q_y / h, T, h + z_g$$

To force the diffusion terms to be conservative, when the $i+1$ node or the $i-1$ node is land, then the i value is used in its place.

UNCLASSIFIED

UNCLASSIFIED

The CFL condition on the vertically integrated hydrodynamic equations limits the time step to:

$$\Delta t = \left[(gH)(\Delta x^{-2} + \Delta y^{-2}) \right]^{-1/2} \quad (57)$$

where H is the maximum depth in the domain. Trial and error testing show that (57) must be multiplied by 0.13 to ensure a stable and accurate solution. The latest timestep is not allowed to increase by more than 10% from the previous timestep. The code automatically sets its own timesteps, with no input from the user.

All terms in Eqs. (1) - (5) except for the vertical diffusion terms are solved one horizontal layer at a time, starting at the bottom. The vertical velocities are computed on a staggered grid as a part of this process, starting with a lower boundary condition (usually zero) at the bottom of the lowest slab.

Since the 3-D system is not subject to the more restrictive stability criterion associated with free surface waves, longer timesteps can be used when solving that system. The constraint used is 20% of the Courant limit on the fastest horizontal velocity in the model domain. We found that this constraint allows about ten timesteps for the 2-D system before the 3-D system must be updated. We found that a less restrictive constraint on the 3-D system timestep caused the solution to become noisy and unstable. Although a 20% limit on the Courant limit for the 3-D system appears very restrictive, it allows the 3-D system timestep to be about ten times longer than the 2-D system timestep, which reduces running time tremendously relative to the times required if both the 2-D and 3-D systems are solved using timestep imposed by free surface gravity waves.

The systems (1)-(5) and (49)-(51) are solved by first marching through (1)-(5) using values of h computed at the previous time step. Then new vertically integrated values of u and v are computed and used to start the integration of (49)-(51). After about ten short time steps, the integration of (49)-(51) is stopped, and the new values of h are used in (1)-(5) to march forward one longer time step (equal to the ten short time steps). Then this process is repeated, using new vertically integrated values of u and v to compute new values of h. Starting each integration of (49)-(51) with new vertically integrated values of u and v derived from the most recent 3-D values of u and v links the systems (1)-(5) and (49)-(51). This direct linkage means that no adjustments of either the 2-D or 3-D velocity fields are needed to ensure mass conservation. Jin and Kranenburg (1993) and Johnson et al (1993) have to make small but continuous adjustments to their computed velocity fields because they retain separate 2-D (vertically integrated) and 3-D values of u and v in their numerical integrations.

UNCLASSIFIED

UNCLASSIFIED

The vertical diffusion terms in Eqs. (1), (2) and (3) are solved separately (time-splitting) using a semi-implicit Crank-Nicholson technique (Press et al, 1992).

3.2 Boundary Conditions

The user has three options for lateral (inflow or outflow) boundary conditions. In the array IGRID.DAT, if 8's are put in the inflow/outflow positions at the edge of the grid, then zero-gradient boundary conditions for temperature and velocity will be used, unless the normal velocity component one cell from the boundary is directed inward from the boundary. In that case, the normal velocity component will be set to zero. If 9's are put in the inflow/outflow positions, then zero-gradient boundary conditions are used everywhere. If 1's are put in the inflow/outflow positions, then the temperatures and velocities at those boundary locations will remain fixed throughout the simulation at their initial values. The user can mix these different types of boundary conditions, but if that is done, the user should make sure that the mixture is physically realistic.

The water depth (h) at the boundaries is fixed at its initial value unless a tidal simulation is being performed. In that case, 9's should be used at all nodes representing water at the edge of the grid. As described below in Section 4.3, an input file named PERAMP.DAT provides tidal period and amplitude data that ALGE uses to impose a sinusoidally varying water depth at the edge of the grid.

As described in Section 2.0, the upper boundary of the model is a free surface, and in the uppermost layer of the model wind stress and convective, evaporation and radiative (solar and thermal wavelengths) terms are added to the equations to simulate momentum and energy transfer from and to the atmosphere. At the bottom layer, a logarithmic relationship (Eq. 11) is used to compute a current speed at a level that is one-half of the vertical mesh size (0.5dz) above the bottom. This speed is used for the lower boundary values in the Crank-Nicholson integration of the vertical diffusion terms in Eqs. (1) - (3).

3.3 Nudging

As shown in Section 5.1, ALGE can compute tidal currents within bays and estuaries, given the forcing from the open ocean. The entire bay must be resolved within the model domain in order to make accurate tidal flow calculations. Typical resolutions are on the order of one kilometer. Typical resolutions for simulations of thermal plumes are on the order of 10 m. Thus model resolution must increase by two orders of magnitude to accurately track a thermal plume in a bay after the general pattern of currents has been calculated. It is not feasible to increase the resolution this much over the entire bay. Instead,

UNCLASSIFIED

UNCLASSIFIED

the large scale solution is used to drive a high resolution, limited area simulation of the thermal plume via a technique known as nudging.

Nudging is a form of four-dimensional-data-assimilation (FDDA) extensively used by atmospheric modelers (Stauffer and Seaman 1990). The concept is illustrated for some variable α which is governed by the following conservation equation:

$$\frac{\partial \alpha}{\partial t} = F(\alpha, x_i, t) + G_\alpha W(x_i, t)(\alpha_N - \alpha) \quad (58)$$

where F represents all terms except for the nudging term (such as advection, pressure, Coriolis); G_α is the nudging factor, which has units of 1/time; W is a weighting function and α_N is the value that α is being nudged to. The nudging factor determines the rate at which α will approach α_N . For this work, a value of G_α of 0.003 s^{-1} is used. This is somewhat larger than the values typically used in atmospheric modeling (0.0001 to 0.001 s^{-1} , Stauffer and Seaman 1990), but the mesh sizes and scales of motion are smaller, so a larger value (more rapid nudging) appears appropriate. The exact value of the nudging factor for this application probably is not critical, because the nudging terms provide most of the forcing. So as long as the nudging does not cause numerical instability, the final result (for steady-state nudging) should be the same.

The weighting factor W in this application decreases the magnitude of the nudging factor at nodes close to shore. This is done to avoid the physically unrealistic condition of forcing velocities appropriate for open waters away from shore at locations close to shore.

- * Nudging applied to limited-area tidal current analysis essentially amounts to generation of a dynamically and mass consistent flow field from a first guess field derived from some other model or analysis (in this application the coarse resolution ALGE run). The first guess at each model node is a weighted average of all α_N in the model domain. Simple $1/R^2$ weighting is used to generate the fields.

The vertical profile of the nudged velocities is computed according to:

$$U_{ni} = \zeta U_n \quad (59)$$

where U_{ni} is the nudging velocity at some level i , U_n is the surface (maximum) nudging velocity and ζ is defined by:

UNCLASSIFIED

UNCLASSIFIED

$$\zeta = \frac{\ln[(h - z_i) / z_o]}{\ln[h / z_o]} \quad (60)$$

where the depth z_i is measured downward from the surface.

4.0 INPUTS FOR NUMERICAL SIMULATIONS

ALGE requires several types of inputs:

- Surface meteorological data
- Upper air meteorological data
- Tidal forcing (when needed), amplitudes and periods \times
- Land/water distribution
- Water depths
- Miscellaneous data, e.g., mesh size, start time, Julian day, roughness, latitude, longitude

These inputs are described below.

4.1 Surface Meteorological Data

ALGE uses hourly surface meteorological data. ALGE can accept up to 200 hours of surface data, which is prepared by MET.F. The variables prepared by MET.F are: wind direction (deg), wind speed (m/s), temperature (K), dewpoint temperature (K), cloud cover (0.0 to 1.0), cloud height (km) and pressure (mb). MET.F uses a cubic spline routine to generate hourly data from observations taken at 6 hour intervals. ALGE reads in the input from MET.F as an array identified as SFC.DAT.

4.2 Upper Air Meteorological Data

ALGE uses upper air data interpolated to hourly values. ALGE can accept up to 200 hours of upper air data, which is prepared by UPP.F. The variables prepared by UPP.F are: temperature and precipitable water (cm). Temperature is read in °C and converted to K. ALGE expects the upper air data to be spaced in 12 hour intervals. UPP.F uses a cubic spline routine to generate hourly data from the 12 hour rawinsonde data. The first observational height is assumed to be 100 m, and then reported heights are to be at 1 km, 2 km and so on. ALGE reads in the input from UPP.F as an array identified as SND.DAT.

UNCLASSIFIED

UNCLASSIFIED

4.3 Tidal Forcing

The tidal forcing controls ALGE's estuarine simulations (winds and mass sources and sinks are minor perturbations in most cases). In order to simulate flows driven by tidal forcing, time-dependent sea surface heights must be provided as an input file to ALGE. The National Oceanic and Atmospheric Administration (NOAA) provides Tide Tables and Tidal Current Tables for many locations throughout the world, including the east coast of the U.S. These tables contain daily predictions of the times of high and low tides, tidal amplitudes, maximum and minimum tidal current speeds and directions and the times of those maxima and minima. The predictions are based on statistical analyses of years of data at the different monitoring stations maintained by NOAA and are a good source of boundary condition data for tidal simulations. In the 3-D ALGE simulations described in this report, the tidal amplitudes as reported by NOAA are not modified prior to use as inputs to the code. This is an advantage over 2-D ALGE (Garrett, 1994), which required a 50% increase in the NOAA amplitudes in order to reproduce the observed current speeds.

The variation in forcing at the boundary is modeled by a simple sine function:

$$h_B(t) - h_m = A \sin(c_t t_p) \quad (61)$$

where A is tidal amplitude (one-half of range), h_B is the depth at the boundary, h_m is the mean water depth, t_p is a time variable and c_t is defined by:

$$c_t = \pi / P \quad (62)$$

where P is half a semi-diurnal period ($P \sim 6$ hours). The values of P and A are provided by NOAA (1994), and must be updated each time a low or high tide is passed, because they are not constants. The use of a sine function to interpolate between successive values of P and A is recommended by NOAA. Since ALGE's estuarine simulations are always started with uniform water surface levels ($h = h_m$ everywhere), it is convenient to compute h_B by differentiating (61):

$$\frac{dh_B}{dt} = A \cos(c_t t_p) c_t \quad (63)$$

Putting (63) into finite difference form:

$$h_B(t^{n+1}) = h_B(t^n) + \Delta t A \cos(c_t t_p^{n+1}) c_t \quad (64)$$

At the beginning of each approximate six hour period, t is initialized as $t_p = P/2$, thus, $\cos(c_t t_p)$ varies from 0 to -1 and back to 0 as t ranges from $P/2$ to P to $1.5P$.

UNCLASSIFIED

UNCLASSIFIED

Since all simulations start with $h=h_m$, or about three hours through a rising tide, at the beginning of a simulation $t_p = 0$. This causes $\cos(c_t t_p)$ to start out =1, and finish the (approximate) first three hours $(0.5P) = 0$. For the next period of about six hours, h will decrease, since $\cos(c_t t_p)$ is always less than or equal to zero. Resetting P and A after each high and low tide requires t_p to be reset to $P/2$ each time, so for all successive odd periods ($P=3,5,\dots$), the amplitudes (A 's) are negative, to produce alternating rising and falling tides.

The tidal forcing data are read in by ALGE in an array identified as PERAMP.DAT. An example is given below:

6 *k = 6 periods*
1.31,1.28,-1.17,1.22,-1.32,1.32
6.52,6.08,6.25,5.97,6.45,6.05

The first line gives the number of periods between high and low tides (6) covering approximately 36 hours. The second line gives the amplitude (deviation from mean sea surface elevation) in meters. The third line gives the duration of the period in hours.

4.4 Land-Water Distribution

ALGE uses a 2-D array called $ID(x,y)$ to identify nodes that represent land (0's) and nodes that represent water (1's). ALGE assumes that all non-zero numbers are water. Special locations over water are: mass and energy sources (7's), mass and energy sinks (6's), inflow and outflow boundaries (8's and 9's) and nodes for which time series data are to be saved (2's). These data are read in by ALGE in an array identified as IGRID.DAT.

4.5 Water Depths

Water depths are read into ALGE via a file called IDEPTH.DAT. This file contains one integer per node, ranging from 0 to 9. As in igrid.dat, zero's refer to land nodes. Digits 1 through 9 and alphanumeric characters a through z define the number of levels at a horizontal (x,y) location (maximum of 35). The depth at an (x,y) location is defined by the product of this number and the vertical grid mesh, which is contained in the PARAM.DAT file.

4.6 Nudging Inputs

Inputs for nudging consist of time series of hourly velocity components (u,v) at three locations in the model domain. These data are stored in the input file NDG.DAT. The velocity components in NDG.DAT are surface velocities, the nudging velocities below the surface are computed during the simulation

UNCLASSIFIED

UNCLASSIFIED

according to the procedure described in Section 3.3. The weighting function W (Section 3.3) is computed with the code WEIGHT.F, which generates an output file that is named WGTAR.DAT. If the nudging flag is on in PARAM.DAT, then ALGE will expect to read both NDG.DAT and WGTAR.DAT along with the other input files.

4.7 Other Input Parameters

Other input parameters are contained in PARAM.DAT; including horizontal and vertical grid spacing, start time, total simulation time, latitude, longitude, Julian day, bottom roughness length, boundary inflow and outflow temperatures, mass source temperature, mass source and sink flow rates, angle of x-axis from north, print interval, numbers of nodes in x and y directions, reference height for heat transfer to atmosphere, bottom slope angles (used for river simulations), initial time step size, initial magnitudes of velocity components, and flags for time interval between heat transfer updates, vertical level of mass source, use of nudging, heat transfer and outfall temperature.

5.0 BENCHMARKING AND SAMPLE SIMULATIONS

5.1 Delaware Bay

5.1.1 Baseline Simulation

Delaware Bay was selected to test ALGE's estuarine tidal predictions because it experiences fairly large tidal amplitude and velocity oscillations and a large number of observation stations are located throughout the bay (see Fig. 5.1.1). The simulations are based on depths drawn from maps provided by the University of South Carolina Geography Department. No one map was a good candidate for digitizing (because none were complete maps of the bay, and they were different sizes). The depth array (Fig. 5.1.2) derived from these maps was therefore a manual digitization, and could be made more accurate if a better source of bathymetric data becomes available. The mesh (0.67 km north-south, 0.6 km east-west) smoothed out the finer-scale detail on the maps. As discussed below, this smoothing may have been responsible for some the differences between observed and computed tidal current speeds and directions.

Figure 5.1.3 and 5.1.4 show surface flow fields and sea surface elevation (departures from mean elevation defined as zero) 14 and 20 hours into a 33 hour simulation of tidal currents in Delaware Bay on February 24-25, 1994. The computational grid had 177 nodes in the north-south (top to bottom of figure) direction, 112 nodes in the east-west direction and 9 nodes on the vertical axis. The velocity vectors are averages over 2x2 blocks of nodes. The sea surface

UNCLASSIFIED

UNCLASSIFIED

elevation contours were plotted from unaveraged data. The crooked lines projecting from the left (west) shore of the Bay in the figures are simulated tidal creeks. These were included in the simulation because some of the NOAA stations are at the mouths of these creeks, which affect the measured speeds and directions. The lowest tidal creek in Fig. 5.1.3 appears to be separated from the Bay as a result of the averaging of the data and the graphics software. Fig. 5.1.3 shows an incoming tide in the lower two-thirds of the Bay, with a falling (ebbing) tide still in progress in the upper third of the bay. Large bays can contain much or all of an entire tidal cycle at one time, which illustrates why it is necessary to use simulation to fill out the entire flow field for transport studies. Even in data-rich regions such as Delaware Bay, the observations are only sufficient for benchmarking and boundary conditions for simulations. The current speeds corresponding to the velocity vectors in Fig. 5.1.3 range from near zero to 1.4 m/s (Fig. 5.1.5), with the greatest speeds in the mouth of the bay where the flow is constricted. The current speed contours in Fig. 5.1.5 were computed from unaveraged data. Note that there are velocity maxima associated with the ebbing tide in the northern part of the bay, and with the flooding tide in the south, with a slack tide between. Clearly, there is never a steady-state flow field in areas dominated by tidal currents.

Six hours later, the flow field has reversed (Fig. 5.1.4) with ebbing tide in the lower two-thirds of the bay, and the remnant of the earlier flood tide in the upper part of the bay. Velocities are again highest in the mouth of the bay (Fig. 5.1.6), where speeds as high as 1.6 m/s are predicted near the west side of the mouth. There is another, slightly lower velocity maxima on the east side of the mouth. Highest tidal velocities on the sides of openings to estuaries is a commonly observed feature of these systems (Blanton, 1995).

Fig. 5.1.7 shows vertical crossections (running west to east) of current speed about 10 km north of the mouth and in the mouth of the bay. NOAA measurements of vertical velocity profiles are limited, but the type of information available is shown in Table 1 below. The ratios in Tables 1 are ratios of speeds measured by sensors near the bottom to measurements at depths of 4 to 6 m. The average speed near the bottom is one-half to two-thirds the average speed nearer the surface.

UNCLASSIFIED

UNCLASSIFIED

Table 1
Variation of Speed with Depth in Delaware Bay

STATION	FLOOD SPEED RATIO	EBB SPEED RATIO	DEPTHS (FT)
Cape May	0.8	0.7	15/25
Cape Henlopen #1	0.6	0.3	12/70
Cape Henlopen #2	0.6	0.6	18/28
Brandywine #1	0.7	0.6	15/45
Brandywine #2	0.6	0.5	15/40
14 Ft. Bank	0.8	0.6	12/30
Ben Davis Pt.	0.4	0.2	12/43
Arnold Pt.	0.8	0.7	14/29
Averages	0.66	0.52	

Referring back to Fig. 5.1.7, the computed velocity profiles show a gradual decrease down to the lowest model layer, and then a rapid decrease. The data in Table 1 appear to show a similar but possibly more gradual decrease in speed with depth, but the variability is so great and the number of observations so limited that quantitative comparisons are not meaningful.

Quantitative comparisons can be made between observed and computed lag times for low and high tides from the mouth of the bay to the upper end (Figs. 5.1.8 and 5.1.9). NOAA provides statistical information about the accuracy of predicted times of high and low tides in its tables. For example, NOAA states that its high water predictions will be correct to within 0.4 hours (24 minutes) 90% of the time at Breakwater Harbor near the entrance to Delaware Bay. For low tides the claimed accuracy is 0.3 hours (18 minutes) 90% of the time. For Reedy Point, which is at the upper end of the Bay, the stated accuracies are 0.4 hours (24 minutes) and 0.5 hours (30 minutes), respectively.

Fig. 5.1.8 compares the NOAA data on lag times for high tides in Delaware Bay to ALGE's predictions. The lag times are referenced to Breakwater Harbor, which is station 1877 in Fig. 5.1.1. Note that in general the lag time increases with distance from the entrance to the Bay, as expected. ALGE and the NOAA data agree to within a few minutes for all stations, except for Station 1887, which is at the mouth of a tidal creek, and Station 1875. The discrepancy between predicted and observed time of high tide at Station 1887 is 22 minutes, which is still within the observational scatter (90%). The 21 minute discrepancy at Station 1875 may have been caused by the proximity of the model domain boundary

UNCLASSIFIED

UNCLASSIFIED

combined with the effects of averaging over the highly variable depth distribution in the vicinity of the mouth of the bay.

The results are similar for the ebb tide lag predictions (Fig. 5.1.9), with the only notable discrepancy again at Station 1875. The computed time of low tide led the observed time by 34 minutes in this case. The next largest discrepancy of 22 minutes was at Station 1867, and this is within the scatter of the data reported by NOAA.

Taken together, Figs. 5.1.8 and 5.1.9 show that ALGE handles the basic problem of propagating a tidal wave through a body of water with complex boundaries and depth distributions. A single roughness length of 0.01 m was used over the whole domain. A roughness length of 0.01 m is fairly small, particularly when it is considered that the model resolution of about 0.6 km eliminates smaller scale topographic variability at the bottom of the bay. Small ridges and other local surface irregularities increase the effective surface roughness length in the atmosphere (Taylor et al, 1989, Grant and Mason, 1990), and must have the same effect in water. In contrast, Johnson et al (1993) found that a roughness length of 6.7×10^{-4} m gave best results in their Chesapeake Bay simulations. The source of this discrepancy is unknown. Later in this section, we present some additional simulation results which quantify the sensitivity of ALGE to changes in roughness length.

Fig. 5.1.10 compares ALGE maximum tidal current speed predictions to NOAA data for flooding (incoming) tides. Current speeds and directions will be more affected by local depth variations and obstacles such as jetties than tidal depths. Even the computed distributions of current speeds are highly variable (refer back to Figs. 5.15 and 5.16). In Fig. 5.1.10, we see that the speeds are fairly accurately predicted by ALGE except for Stations 1871, 1877 and 1881. Stations 1877 and 1881 are located at the mouths of tidal creeks, which are only coarsely resolved by ALGE. The tidal creeks affect local current speeds and directions and higher resolution would be necessary to get better agreement. Even with higher resolution, some discrepancies are likely because very small unresolvable features can affect point current measurements. Station 1871 is out in the middle of the bay (see Fig. 5.1.1), and this discrepancy may be due to very shallow reefs that with minimum depths of 1 m on either side of this station. The water below Station 1871 is 10 to 12 m deep, and the change in depth to the reefs on both sides is very rapid and was not resolved in these ALGE simulations. The reefs may channel both flooding and ebbing tides, which would lead to local acceleration of the flow near Station 1871. In spite of these individual discrepancies, the average of the eight observed current speeds in Fig. 5.1.10 is 0.76 m/s, compared to an average of 0.74 m/s for the computed speeds.

UNCLASSIFIED

UNCLASSIFIED

Fig. 5.1.11 compares ALGE maximum tidal current speed predictions to NOAA data for ebbing (outgoing) tides. Overall, the agreement between observed and computed speeds looks a little better. The discrepancies at Stations 1877 and 1881 are smaller, although they are a little larger at Stations 1885 and 1871. The average observed current speed for the eight stations is 0.88 m/s, compared to an average of 0.83 m/s for the computed speeds, so again the averages are close.

NOAA also provides the measured directions of the current during flood and ebb tides (Figs. 5.1.12 and 5.1.13). Agreement between observed and computed directions is worst for the stations at the mouths of the tidal creeks, which is not surprising. The largest discrepancies are at Stations 1881 and 1885, so these stations were selected for additional analysis. Plots of flow vectors in the areas of those stations are shown in Figs. 5.1.14 and 5.1.15. Unlike Figs. 5.1.3 and 5.1.4, these plots were created from unaveraged ALGE output and show more details of the flow.

At Station 1881 for flooding tide (Fig. 5.1.14), the observed direction is about 210° , and the computed direction is about 140° . The computed direction looks reasonable when checked against the actual coastline and creek configuration in Fig. 5.1.1, if the flow at Station 1881 reflects flow going into the tidal creek. But apparently Station 1881 is not affected by the tidal creek, and the slightly northeast turn to the coastline near Station 1881 must force the flow to move to the north-northeast (from the south-southwest). The north-northeast turn of the coastline is not resolved by the ALGE grid. However, note that just south of the computed velocity vector in Fig. 5.1.14, the flow is from about 180° , which is much closer to the observed direction of 210° . At Station 1885, the computed direction is from 70° , which indicates inward flow at the node at the mouth of the simulated tidal creek. The observed direction is 150° , which indicates that Station 1885 is outside the influence area of the tidal creek and its current direction is controlled by the flow in the open bay, which is toward the north-northwest during a flooding tide.

For the ebbing tide (Fig. 5.1.15), the observed direction at Station 1881 is from about 10° , whereas the computed direction is from 285° . This discrepancy again appears to have been caused by the location of Station 1881, which must be far enough out into the bay to not be influenced by the tidal creek. The difference between the computed and observed directions at Station 1885 is not large, and again is probably caused by a station location that is somewhat seaward of the mouth of the tidal creek.

There is about a 50° discrepancy between the observed and computed directions at Station 1879 for an ebbing tide. Uncertainty about the station location relative to the mouth of the tidal creek and grid resolution are again probably responsible.

UNCLASSIFIED

UNCLASSIFIED

Observed and computed tidal amplitudes are compared in Figs. 5.1.16 (high tide) and 5.1.17 (low tide). At high tide, the observed and computed amplitudes correlate well and the average observed amplitude is 0.94 m and the average computed amplitude is 0.89 m. For some reason, the observed and computed amplitudes do not correlate as well at low tide, with more station-to-station variability evident in the observed amplitudes and less in the computed amplitudes. However, the average computed amplitude is -0.91 m, which is close to the -0.95 m observed amplitude. Note that Stations 1883 and 1885 are very close to each other (Fig. 5.1.1) and have nearly the same amplitude at high tide, but are different by nearly 0.2 m at low tide. This asymmetric behavior must be due to local topographic features.

5.1.2 Sensitivity to Magnitude of Roughness Length

Section 5.1.1 showed that ALGE reproduces observed tidal velocities and amplitudes and propagates the tidal wave at the correct speed through Delaware Bay. The roughness length used in this simulation was 0.01 m. Since this was a reasonable but arbitrary value that produced good results, it is appropriate to determine how sensitive the simulations are to different roughness lengths. So we ran another simulation with a roughness length of 0.001 m, which is close to the value ($6.7\text{e-}4$ m) used by Johnson et al (1993) in their simulations of Chesapeake Bay.

The simulation with a roughness length of 0.001 m did not do quite as good a job of predicting the movement of the tidal wave through the bay (Fig. 5.1.18) and Fig. 5.1.19). The average computed amplitude of 1.03 m for high tide is larger than the observed amplitude of 0.94 m, and the average computed low tide amplitude of -1.03 m was also larger than the observed value of -0.95 m. The average computed current speed during flood tide rose to 0.82 m/s, a little larger than the observed value of 0.76 m/s. The average computed current speed during ebb tide rose to 0.95 m/s, again a little larger than the observed speed of 0.88 m/s. The computed directions changed very little from those computed in the simulation with a 0.01 m roughness length. Although the results from the simulation with the 0.001 roughness length are overall not quite as good as the results from the simulation that used 0.01 m, they are not very different, considering the order of magnitude change in roughness length. This implies that fairly accurate simulations are achievable at locations where numerous observations are not available, as long as reasonable estimates of parameters such as roughness length are used.

Again we note that the effective roughness length depends on the model resolution because that determines how much smoothing of the local topography there is. If the mesh is coarse, then the roughness length must be increased to

UNCLASSIFIED

UNCLASSIFIED

account for larger features that act as roughness elements but which are not resolved in the simulation.

5.2 SRS Pond "C" Analysis

Pond C is a 130 acre (0.53 sq. km) cooling lake at SRS that received heated water from P Reactor when it operated. Pond C functioned as a pre-cooler for Par Pond (see Figure 5.2.1). It typically received a flow of about 180,000 gpm ($11.4 \text{ m}^3/\text{s}$) water at about 50°C . The area of Pond C is small relative to this heat load, so the water exiting Pond C via a submerged pipe at the lower end was still much hotter than ambient temperatures. For this reason, strong thermal gradients existed in Pond C when P Reactor was operating, and buoyancy forces had a large impact on the flow patterns in addition to the forced flow of $11.4 \text{ m}^3/\text{s}$ through the pond. Figure 5.2.2 shows the temperature distribution ($^\circ\text{C}$) in Pond C at about noon on April 2, 1984, derived from EG&G overflight imagery and surface temperature measurements (Garrett, Hayes and McMillan, 1984). The exact time that the image was taken is not known. The imagery data were averaged in cells about 24 m on a side.

Based on the direct surface measurements, it appears that the strong near-shore temperature gradients in Fig. 5.2.2 are at least partly artifacts of the imagery. Some pixels cross the water-land boundary, and thus combine cooler land temperatures with the warmer water. This mixed data is present in the averaged information shown in Figure 5.2.2, but only in cells immediately adjacent to land. These contaminated cells were not included when simple statistical measures of skill such as bias, root-mean-square-error (RMSE) and correlation coefficient were computed to quantify the accuracy of ALGE's simulation (see following paragraphs).

The arm of Pond C that extends to the upper right hand corner of Figure 5.2.2 has no outlet. It is clear that buoyancy forces were pushing water into this dead-end arm of Pond C, and that the water cooled and sank at the upper end and returned as a bottom flow. Some of the bottom flow went out the submerged pipe, and some returned to the outfall region where it mixed with the incoming flow. Most of the mixing apparently happened as the hot water entered the main body of the pond, and not in the small arm on the upper left which received water from P Reactor. (Note that the strongest temperature gradients are in the upper middle part of Pond C, between the upper left and upper right arms. This implies that much of the mixing with cooler bottom water was happening there, rather than at the inlet to the pond.)

The corresponding simulated surface temperatures and velocity vectors by ALGE are shown in Figure 5.2.3. The results shown are from a 24 hour simulation that used the actual flow rate of $11.4 \text{ m}^3/\text{s}$, outfall temperature and

UNCLASSIFIED

UNCLASSIFIED

observed meteorology (winds, temperatures, humidities, cloud cover) in the computation of sensible, latent and radiative energy fluxes from the surface of the pond to the atmosphere. The pond depths were based on direct measurements (Garrett, Hayes and McMillan, 1984). The overall temperature distribution is similar to the observed distribution, but smoother. This is to be expected, because there is no time averaging in the image, whereas ALGE predicts time and space averaged temperature distributions. The most notable discrepancy between simulation and observation is in the upper part of the main body of the pond, between the left and right arms. The observed temperature gradients in that area are skewed down toward the lower end of the pond, whereas the computed contours are skewed toward the dead arm in the upper right. The difference appears to have been caused by the response of the simulated pond to the wind stress. The winds at the time the thermal image was made were 4 to 5 m/s from the south, which would tend to force warm surface water into the dead arm. The real pond did not respond to the wind stress to the same degree. Since the pond is surrounded by tall trees and the land on the west side of the pond is elevated, it may be that the west side of the pond was sheltered from the wind to a significant degree. This sheltering would allow buoyancy forces to drive more of the warm surface water toward the lower end of the lake, rather than toward the dead arm.

In spite of the differences in contour configuration, the temperature distribution predicted by ALGE overall is very similar to the observed distribution, as shown by the following simple statistical measures of skill (based on 752 pairs of observed and predicted temperatures). Also shown are the same statistics from the 2-D version of ALGE (Garrett, 1994).

Code	Correlation Coefficient	Bias (°C)	RMSE (°C)
ALGE-2D	0.90	1.1	1.7
ALGE-3D	0.76	0.1	1.9

With the exception of the bias, the results from ALGE-2D are slightly better than the 3-D results, although the differences between the results from the two versions of ALGE for all three measures of skill are physically insignificant. It is not surprising that the ALGE-2D results are about as good as the 3-D results for a cooling pond, because the distributed mass sink approximation to 3-D flow used by ALGE-2D produces a flow field that is similar to the flow field generated by a 3-D code. However, the 3-D version of ALGE is easier to use, because it is not necessary for the code user to input a thermal layer depth or an outfall mixing coefficient, both of which must be guessed if site-specific data is not available.

UNCLASSIFIED

UNCLASSIFIED

Since the numerical simulation does appear to be a fairly good approximation to reality, it is of interest to see if the computed subsurface circulation verifies the assertion that warm surface water flows into the dead arm cooled and returned to the main body of the pond underneath the surface. Figs. 5.2.4 and 5.2.5 show velocity vectors and temperature contours at two subsurface levels in the simulation (2.0 and 4.0 m). Comparing surface flow and temperatures (Fig. 5.2.3) to the same variables at a 2 m depth, we see that the flow has already reversed in the cold arm and is heading back to the main body of the lake. Some of the return flow goes all the way back to the outfall, where it mixes with hot water coming into the pond. The rest of the flow heads down the lake and is either entrained and recirculated (see Fig. 5.2.5) or it exits via the mass sink at the bottom near the lower end of the lake. Also note that there is some subsurface return flow from the smaller dead arm in the lower left end of the pond. Return flow from both dead arms is apparent in Fig. 5.2.5. These return flows both head towards the upper middle part of the lake, where some of this cooler subsurface water returns to the outfall to mix and recirculate, and some is entrained along the way and flows back down the lake toward the mass sink. It is clear that the computed circulation is highly three dimensional, with flow moving in and out of the individual horizontal planes shown in Figs. 5.2.3, 5.2.4 and 5.2.5.

In order to test the hypotheses that sheltering along the western (left) shore of the pond caused the difference in contour configuration between Figs. 5.2.2 and 5.2.3, another simulation was run with winds from the west-northwest, but with all other inputs the same (Fig. 5.2.6). This wind direction tends to blow the hot water down the lake to a greater degree, with a corresponding reduction in the flow to the upper right dead arm. The change in the wind direction produced contours more like those in Fig. 5.2.2. The reduction in flow to the cold arm caused the average computed temperature to drop 0.6°C below the observed average (-0.6°C bias), the correlation coefficient rose slightly to 0.79 and the RMSE rose a little to 2.0°C . So the altered wind direction produced a small subjective improvement, but the quantitative measures of performance hardly changed at all.

5.3 SRS "L" Lake

The SRS L Lake was constructed to receive and cool heated water from L Reactor, and then discharge water at ambient temperatures to the creek leading to the Savannah River. L Lake is about 5.6 km long, and covers approximately 4 km^2 (see Fig. 5.3.1). The outfall from L Reactor entered the left end of the part of L Lake that paralleled the highway at the top of Fig. 5.3.1. High resolution thermal imagery taken by EG&G is only available for the upper part of L Lake, where most of the cooling took place. Fig. 5.3.2 presents averaged temperature data from an image taken at 9:36 AM local time on April 25, 1986. The reactor

UNCLASSIFIED

UNCLASSIFIED

outfall in Fig. 5.3.2 was at the upper part of the 54°C contour. L Lake was shallow near the reactor outfall, and some small islets are apparent in the high resolution imagery that was used to create Fig. 5.3.2. There was a channel that led from the outfall to deeper parts of the lake (see Fig. 5.3.1). A channeling effect is apparent in Fig. 5.3.2, which shows that some of the thermal plume spread out on either side of the outfall, but also shows that much of it flowed along the deeper channel to the far side of the lake and then spread along the shoreline in both directions.

The ALGE simulation of the 4/25/86 L Lake thermal image was performed with a grid that covered the same domain as Fig. 5.3.2, with a resolution of 36.5 m. Since the computational domain for this simulation covered only part of the lake, it is a poorer approximation to reality than the Pond C simulation. This is true primarily because ALGE had to force water to subside at the edge of the computational domain, whereas in the real lake it would have continued to flow at the surface and cool. So the subsurface water in the simulation was warmer than the actual subsurface water.

Fig. 5.3.3 presents the computed temperature distribution for a 40 hour simulation ending at the time that the thermal image in Fig. 5.3.2 was taken. In Fig. 5.3.3 three islets can be seen near the reactor outfall. The islets were included in the simulation based on inspection of high resolution imagery. Their blocking effect on the thermal plume can be clearly seen in Fig. 5.3.2. Note in particular the area of cooler water (38°C contour) in Fig. 5.3.2 near the location of the largest islet in Fig. 5.3.3. The simulated islets did not have nearly as much effect on the computed temperature distribution in Fig. 5.3.3, and this apparently was due to the fairly coarse resolution in the vertical (maximum of 9 layers in deepest part of lake). There was some uncertainty in the depth distribution that was used in the simulation, because available topographic maps of the area before the lake was built are not highly detailed. Except for the channel leading out into the lake from the outfall, the effects on depth distribution of dredging and other work done during and after construction of the lake are not known.

Observed and computed temperatures differ the most in the upper left part of the figures, where the observed temperature is about 27°C and the computed temperature is 29 to 30°C. The wind had just started to blow from the northwest at the time the thermal image was made, which apparently caused upwelling of cooler water in the real lake a little before it did in the simulation. Since the subsurface water in the simulation was warmer than the actual water (as discussed above), the upwelling area is warmer in the simulation.

The same statistical measures of skill were used to compare ALGE predictions to observed temperatures. The same criterion to reject data was used (nodes adjacent to land were rejected because the corresponding locations in the

UNCLASSIFIED

UNCLASSIFIED

thermal image were contaminated to some degree by land temperatures). A total of 978 pairs of predicted and observed temperatures were used to compute the following:

Code	Correlation Coefficient	Bias (°C)	RMSE (°C)
ALGE-2D	0.86	-0.9	3.9
ALGE-3D	0.92	-0.3	3.0

Relative to the results for Pond C, the correlation coefficient and bias are similar and the RMSE is higher, reflecting the lack of channeling in the ALGE simulation that was present in the real lake near the reactor outfall (Fig. 5.3.2). The results from the 2-D version of ALGE (Garrett, 1994) are similar to but not quite as good as the 3-D results, again because the distributed mass sink approximation in the 2-D version produces a surface flow field that is much like the flow field in a 3-D simulation.

5.4 Savannah River

Transport of thermal plumes in the Savannah River is controlled by the current speed, which is usually 0.5 to 1.0 m/s (Kania 1983). The current is determined by the gradient of the river bed, which is about $1.333\text{E-}4$ m/m near and downstream from SRS. The depth of the river near SRS is usually 3 to 5 m, but in some places is as deep as 7 m. The river is a little more than 100 m wide near SRS (Kania 1983).

When SRS reactors were operating, the Savannah River received hot water from creeks that run from the operations areas to the river. Due to concerns about the effects of the hot water on the ecology of the Savannah River, a number of surveys of the creeks were made in the 1980's, e.g., Shines and Doak (1981). Data from a 12/4/83 thermal image of the Savannah River starting at the mouth of Four Mile Creek is shown in Figure 5.4.1. The contours are in °C and about a 0.5 km stretch of the river is represented. Since the hot water traveled several kilometers down Four Mile Creek from C Reactor to the river, it cooled substantially by the time it reached the river. Water leaving the reactors was usually 60°C to 70°C, whereas the water entering the river, as shown in Figure 5.4.1, was about 32°C. Four Mile Creek lost some of its reactor flow to the swamp before reaching the river, so the actual flow rate entering the river from Four Mile Creek was about $8.2 \text{ m}^3/\text{s}$, rather than the nominal $11.4 \text{ m}^3/\text{s}$ (Neill and Babcock 1971).

Since the heated water entering the river from Four Mile Creek traveled through the area represented by the model domain in a few minutes, heat transfer had

UNCLASSIFIED

UNCLASSIFIED

little impact on the plume. The observed temperatures variations downstream were therefore almost entirely caused by shear in the mean flow combined with horizontal and vertical mixing.

Note in Figure 5.4.1 that there are blobs of warmer water along the left bank. These are probably artifacts of the thermal image caused by pixels that were partly over land or trees that leaned out over the river. The data for the small part of Four Mile Creek shown in Figure 5.4.1 obviously were contaminated by trees or land, since the hottest (32°C) water is at the mouth of the creek. The main plume in the river is well-resolved, however, and it stays close to the right bank. As the plume moved downstream, it is apparent that the hottest water moved a short distance out into the river. Further downstream, the horizontal and vertical mixing diluted the plume to the point that it was only 2°C hotter than the rest of the river. We do not know why Figure 5.4.1 shows slightly cooler water in the middle of the river starting about one-third of the way down from the top.

Figure 5.4.2 shows the corresponding ALGE simulation of the Four Mile Creek thermal plume. The grid resolution was 6.1 m and the simulation used a maximum of nine levels in the vertical with a resolution of 0.4 m. We used the data taken by Kania (1983) to create the depth distribution for the simulation. Kania's (1983) data shows that the bottom slopes down gradually with distance from the right shore downstream from the mouth of Four Mile Creek. Further downstream, near the bottom of the computational domain, the bottom slopes much more rapidly with distance from the right shore. This depth distribution was reproduced in the simulation, and it produced about the right decrease in maximum surface temperature with distance downstream in the simulation by first limiting vertical diffusion and then allowing more downstream. In contrast, the 2-D simulation reported by Garrett (1994) kept the maximum temperature too high near the downstream end of the computational domain because there was no vertical diffusion in this simulation. The maximum computed flow speed was 0.7 m/s, which is consistent with the observations by Kania (1983). (Velocity vectors shown are averages over 2×2 blocks of cells.) Also note that the hottest water in the simulated plume remains adjacent to the right bank all the way to the end of the computational domain, whereas the thermal imagery shows that the real plume moved away from the right bank a little. The temperature transect data by Kania (1983) tend to show that observed plume did actually move out a little from the right bank. The tendency for the plume to move out from the right bank may have been caused by the combination of the momentum of the water exiting Four Mile Creek with its buoyancy, which allowed it to slip over the cooler river water. Since Kania's (1983) data also show that the water is very shallow in that area, this all had to happen in water only 1 to 2 m deep. The horizontal and vertical grid resolution in the ALGE simulation was apparently too coarse to capture this detail of the temperature distribution.

UNCLASSIFIED

UNCLASSIFIED

The same statistics computed for the Pond C simulation were computed for the Savannah River simulation and are compared to the 2-D results reported by Garrett (1994). A total of 1146 pairs of observed and predicted temperatures were used to compute the statistics:

Code	Correlation Coefficient	Bias (°C)	RMSE (°C)
ALGE 2-D	0.78	1.3	2.6
ALGE 3-D	0.85	0.1	2.0

The 3-D results are clearly better than the 2-D results, and were more straightforward to produce, because observed depths were inputs to the simulation, rather than a thermal layer depth, which must be guessed or derived from temperature measurements in the body of water being simulated.

5.5 Squaw Creek Reservoir

Texas Utilities Electric Company (TUEC) operates the Comanche Peak nuclear power station in north central Texas near Granbury. The two units produce approximately 2300 MWe when both are operating and discharge about 4350 MW of waste heat into the 13.2 km² (3270 acre) Squaw Creek Reservoir (34.6% efficiency). The Squaw Creek Reservoir is used for recreation, but its primary purpose is dissipation of the waste heat from the reactors. Its temperature is usually well above the temperature of other lakes in the area, because it is rare for both units to be down at the same time. There is little net flow through the lake, but TUEC pumps in additional water from another nearby reservoir if natural flow to the lake is inadequate to replace the water lost to evaporation.

TUEC gave to SRTC plant operating data and August lake temperature survey data for four years of operation (1991, 1992, 1993 and 1994). The 1992 and 1994 data were selected for simulation by ALGE, because they were the most complete data sets and because one unit was operating in 1992, whereas both units were operating in 1994. Figs. 5.5.1 and 5.5.2 are temperature contours drawn from the 1992 and 1994 measurements and Fig. 5.5.3 shows the parts of the lake that were covered in the survey. Although these temperature data are not as comprehensive as the thermal imagery data for the SRS cooling lakes, they do cover enough of the lake for meaningful comparison to simulations. The cooling water intake and discharge for the Comanche Peak plant are also shown in Figs. 5.5.1 and 5.5.2.

Both the 1992 data and the 1994 data show that the hot water leaving the arm of the lake with the discharge tends to remain closer to the bank with the dam

UNCLASSIFIED

UNCLASSIFIED

(stippled area at bottom of both Figures). The warm discharge water continues around to the lower right side of the lake and then moves up the lake, cooling slowly. Vertical temperature profiles show that the lake is very nearly well-mixed down to a depth of about 15 m (50 ft), where there is a thermocline. Some areas of the lake are more than 30 m (100 ft) deep, so about half of the vertical column of water in these areas is within or below the thermocline. Below the thermocline, the water is anoxic, indicating that the lake rarely or never "turns over". So only about the top 15 m of the lake is actively involved in dissipation of the waste heat from the reactor. The 15 m mixed layer depth is unusually large, and can be attributed to the 12m (40 ft) depths of the cooling water intakes and discharges. With a cooling water flow rate of 140 m³/s (2,200,000 gpm) and a surface area of 12.2 km², this gives a mean residence time for cooling of about 15 days. Although this seems like a long time for cooling, the lake has a lot of thermal inertia due to the unusually large depth of the mixed layer. As a result, the water reaching the cooling water intake is still well above the equilibrium temperature. Also, the intake and discharge are both at the lower end of the lake, which helps to keep the intake temperature elevated over equilibrium temperatures. The simulations shown below quantify the impact of the close proximity of the intake and discharge, because they cover the entire lake and thus provide temperature estimates for the upper end of the lake, which is not covered by the surveys.

Fig. 5.5.4 shows contours of predicted temperatures for August 17, 1992, which were generated by ALGE in an eight day simulation that used the observed meteorology for the area over that time period. The simulation started with a uniform temperature of 90°F (32°C) and generated the surface temperature distribution shown in Fig. 5.5.4 after eight days. The predicted temperatures generally are within about 1°F of the observed temperatures over all of the area surveyed. ALGE predicts temperatures about 2°F cooler at the upper end of the lake, relative to the temperatures at the cooling water intake. This is a fairly modest reduction, which indicates that the entire surface area of the lake is dissipating the waste heat. (Additional survey data not shown here support the gradual drop in temperature from the cooling water intake area to the upper end of the lake.) The orientation of the temperature contours in Fig. 5.5.4 show that ALGE correctly predicts that the warm water leaving the hot arm will tend to move across the lower end of the lake and up the right side. Also note that the analyst who drew the contours in Fig. 5.5.1 assumed that there was no drop in temperature in the arms on the lower right side of the lake, since the surveys did not extend into those arms. The ALGE simulation predicted a drop of about 1°F moving from the middle of the lower end of the lake into the arms, which is supported by the additional survey data.

Fig. 5.5.5 shows contours of predicted temperatures for August 11, 1994, which were also generated by ALGE in an eight day simulation using observed

UNCLASSIFIED

UNCLASSIFIED

meteorology. The observed and simulated temperatures are again mostly within about 1°F of each other, with the exception of the upper end of the arm with the cooling water outfall, where there is an area where the simulation is about 2°F too high. Since the outfall is a subsurface jet, local circulations and mixing patterns will exist near the outfall that ALGE cannot not duplicate. But away from the outfall area, the agreement with observed absolute temperatures and the temperature patterns is very good. Since the tendency for the warm water to move along the dam to the lower right side of the lake is observed in the 1992 and the 1994 data, it may be inherent to the dynamics of this cooling lake, rather than a temporary wind-induced pattern. The computed velocity field for the topmost layer of water in the simulation shows that the flow does not turn sharply at the end of the peninsula that contains the discharge. Instead, the momentum of the warm water carries it out to the middle of the lake, where the buoyancy force and the land on the far side slowly turn the current toward the upper end of the lake.

Since the meteorological conditions during August 1992 were similar to the conditions during August 1994, it can be concluded that the differences in observed temperature patterns were mostly due to the factor of two difference in power (one unit versus two on-line). ALGE predicted both observed temperature distributions to within about 1°F, so the Squaw Creek Reservoir data support the conclusion that ALGE can be used to generate fairly accurate power estimates. Since thermal imagery was not available for statistical comparison to the simulations, the accuracy of the power estimates is unknown. But we can say that the natural equilibrium temperature in Squaw Creek Reservoir in August would be close to 85°F. Since the average temperature is about 92°F when one unit is operating, and about 99°F when two units are operating, we can conclude that errors on the order of 1°F correspond to about a 15% error in power estimate for one unit operation, and less than 10% for two unit operation.

In summary, previous sections showed that thermal imagery data over the whole body of water is needed to make the best possible power estimates. But the analysis of the Squaw Creek Reservoir data in this section shows that it is possible to generate fairly accurate power estimates even without comprehensive thermal imagery.

UNCLASSIFIED

UNCLASSIFIED

REFERENCES

Blanton, J. O., 1995: Personal communication.

Blumberg, A. F., and G. L. Mellor, 1983: Diagnostic and prognostic numerical circulation studies of the South Atlantic Bight. *J. Geophys. Res.*, 88, 4579-4592.

Froehlich, D. C., 1989: Finite element surface-water modeling system: two-dimensional flow in a horizontal plane (users manual). Report # FHWA-RD-88-177, U. S. Geological Survey, Water Resources Division, 12201 Sunrise Valley Drive, Reston, VA 22902.

Galperin, B. and S. A. Orszag, 1993: Large Eddy Simulation of Complex Engineering and Geophysical Flows. Cambridge University Press, 600 pp.

Garrett, A. J., 1977: a comparison of the observed longwave radiation flux to calculations based on Kondratyev's and Brunt's methods. *Arch. Met. Geoph. Biokl. Ser. B.*, 25, 127-134.

Garrett, A. J., 1978: Numerical simulations of atmospheric convection over the southeastern U.S. in undisturbed conditions. University of Texas Atmospheric Science Group Report #47, 356 pp.

Garrett, A. J., 1980: Orographic cloud over the eastern slopes of Mauna Loa Volcano, Hawaii, related to insolation and wind. *Mon. Wea. Rev.*, 108, 931-941.

✓ Garrett, A. J. 1982: A parameter study of interactions between convective clouds, the convective boundary layer, and a forested surface. *Mon. Wea. Rev.*, 110, 1041-1059.

Garrett, A. J., 1984: Expected surface layer depths in the L Reactor cooling lake. USDOE DPST-85-204, Savannah River Laboratory, 8 pp. plus figures, tables and appendix.

Garrett, A. J., D. W. Hayes and W. G. McMillan, 1984: Lagrangian and control volume models for prediction of cooling lake performance at SRP. USDOE DPST-84-496, Savannah River Laboratory, 30 pp. plus tables and figures.

✓ Garrett, A. J., and F. G. Smith, III, 1984: Two-dimensional simulations of drainage winds and diffusion compared to observations. *J. Climate Appl. Meteor.*, 23, 597-610.

Garrett, A. J., 1993: Derivation of governing equations for ALGE code. Unpublished notes. Savannah River Technology Center.

UNCLASSIFIED

UNCLASSIFIED

REFERENCES (Contd)

10/12/2001

- Grant, A. L. M., and P. J. Mason, 1990: Observations of boundary-layer structure over complex terrain. *Q. J. R. Meteorol. Soc.*, **116**, 159-186.
- Hicks, B. B., 1972: Some evaluations of drag and bulk transfer coefficients over water bodies of different sizes. *Boundary-Layer Meteor.* **3**, 210-213.
- ✓ Jin, X., and C. Kranenburg, 1993: Quasi-3D numerical modeling of shallow-water circulation. *J. Hyd. Eng.*, **119**, 458-472.
- ✓ Johnson, B. H., K. W. Kim, R. E. Heath, B. B. Hsieh, and H. L. Butler, 1993: Validation of three-dimensional hydrodynamic model of Chesapeake Bay. *J. Hyd. Eng.*, **119**, 2-20.
- Kania, H. J., 1983: Savannah River depth study. Environmental and Chemical Sciences, Inc.
- Kondratyev, K. Y., 1969: *Radiation in the Atmosphere*. Academic Press, 912 pp.
- Louis, J. F., 1979: A parametric model of vertical eddy fluxes in the atmosphere. *Boundary-Layer Meteorol.*, **17**, 187-202.
- National Oceanic and Atmospheric Administration (NOAA), 1994: Tide Tables 1994: East Coast of North and South America. NOAA Distribution Branch, 6501 Lafayette Ave., Riverdale MD, 20737.
- Neill, J. S., and D. F. Babcock, 1971: The dissipation of reactor heat at the Savannah River Plant. DP-1274, Savannah River Laboratory, 105 pp.
- ✓ Oey, L. Y., G. L. Mellor and R. I. Hires, 1985: A three-dimensional simulation of the Hudson-Raritan estuary, Part I: description of the model and model simulations. *J. Phys. Oceanogr.*, **15**, 1676-1692.
- Officer, C. B., 1976: *Physical Oceanography of Estuaries*. John Wiley & Sons, 465 pp.
- Pacanowski, R. C., and S. G. H. Philander, 1981: Parameterization of vertical mixing in numerical models of tropical oceans. *J. Phys. Oceanogr.*, **11**, 1443-1451.
- Phillips, N. A., 1957: A coordinate system having some special advantages for numerical forecasting. *J. Meteorol.*, **14**, 184-185.

UNCLASSIFIED

UNCLASSIFIED

REFERENCES (Contd)

Press, W. H., S. A. Teukolsky, W. T. Vetterling, and B. P. Flannery, 1992: *Numerical Recipes in Fortran..* Cambridge University. Press, Cambridge, 963 pp.

Roache, P. J., 1972: *Computational Fluid Dynamics..* Hermosa Publishers, Albuquerque, NM, 446 pp.

Shines, J. E., and E. L. Doak, 1981: A study of thermal plumes at the Savannah River Plant. EGG-1183-1827, EG&G, Inc., 39 pp.

Smagorinsky, J., 1963: General circulation experiments with the primitive equations, Part I: The basic experiment. *Mon. Wea. Rev.*, **91**, 99-152.

Stauffer, D. R., and N. L. Seaman, 1990: Use of four-dimensional data assimilation in a limited-area mesoscale model. Part I: experiments with synoptic-scale data. *Mon. Wea. Rev.*, **118**, 1250-1277.

Taylor, P. A., R. I. Sykes and P. J. Mason, 1989: On the parameterization of drag over small-scale topography in neutrally-stratified boundary-layer flow. *Boundary-Layer Meteor.*, **48**, 409-422.

UNCLASSIFIED

UNCLASSIFIED

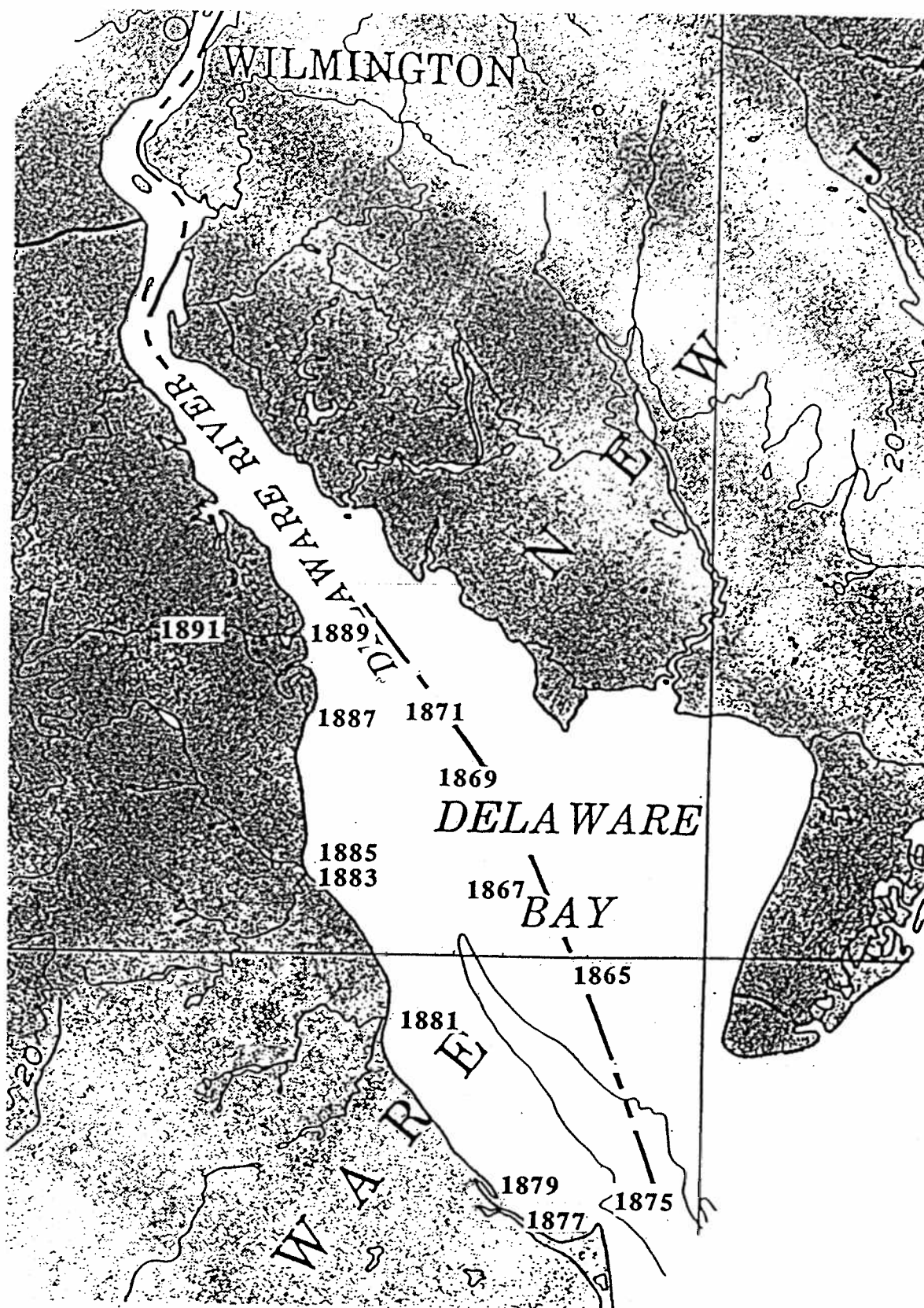


Fig. 5.1.1: Map of Delaware Bay with NOAA tidal measurement stations located by identification numbers

UNCLASSIFIED

UNCLASSIFIED

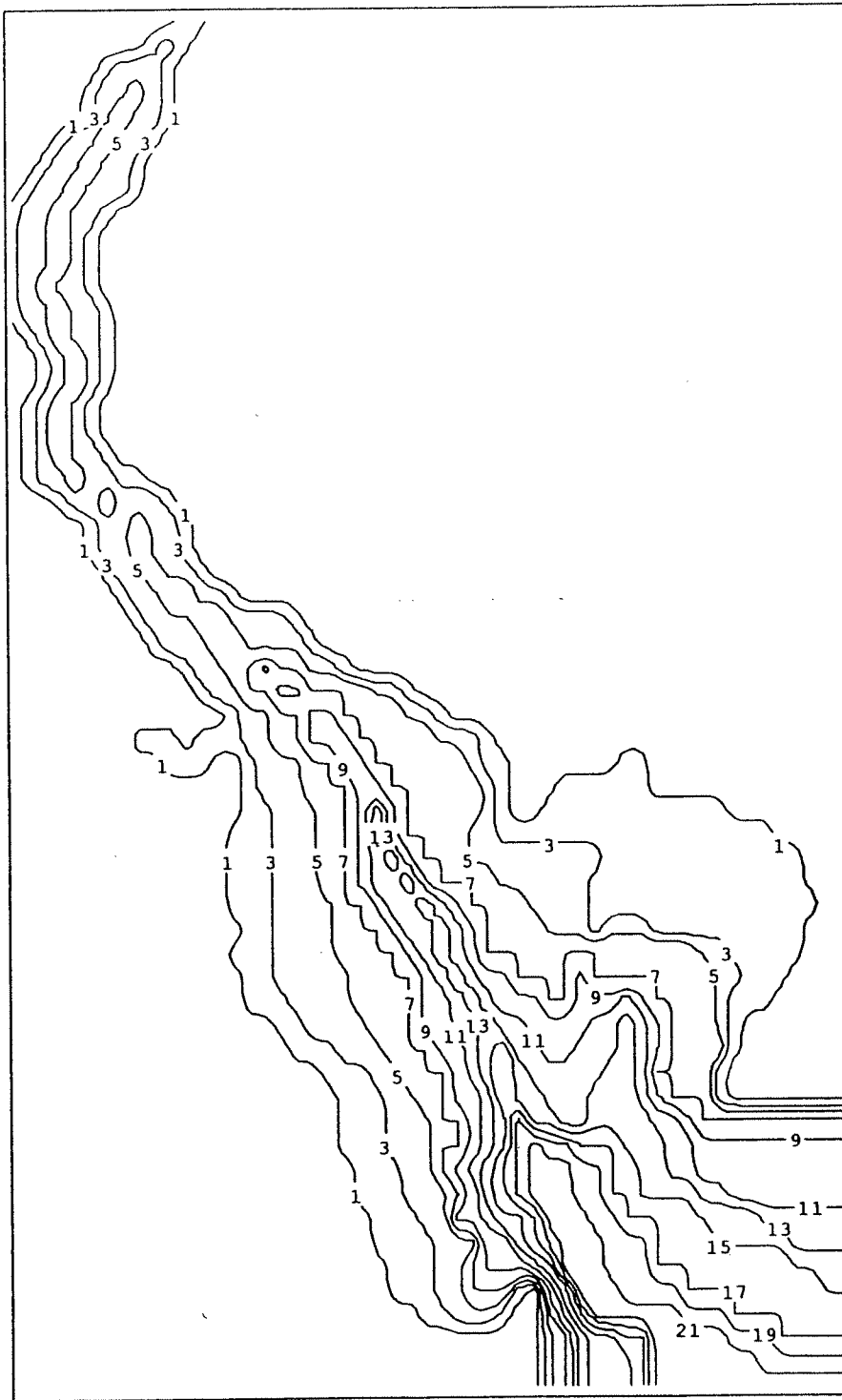


Fig. 5.1.2: Distribution of depths (meters) in Delaware Bay used by ALGE in simulation of tidal currents

UNCLASSIFIED

UNCLASSIFIED

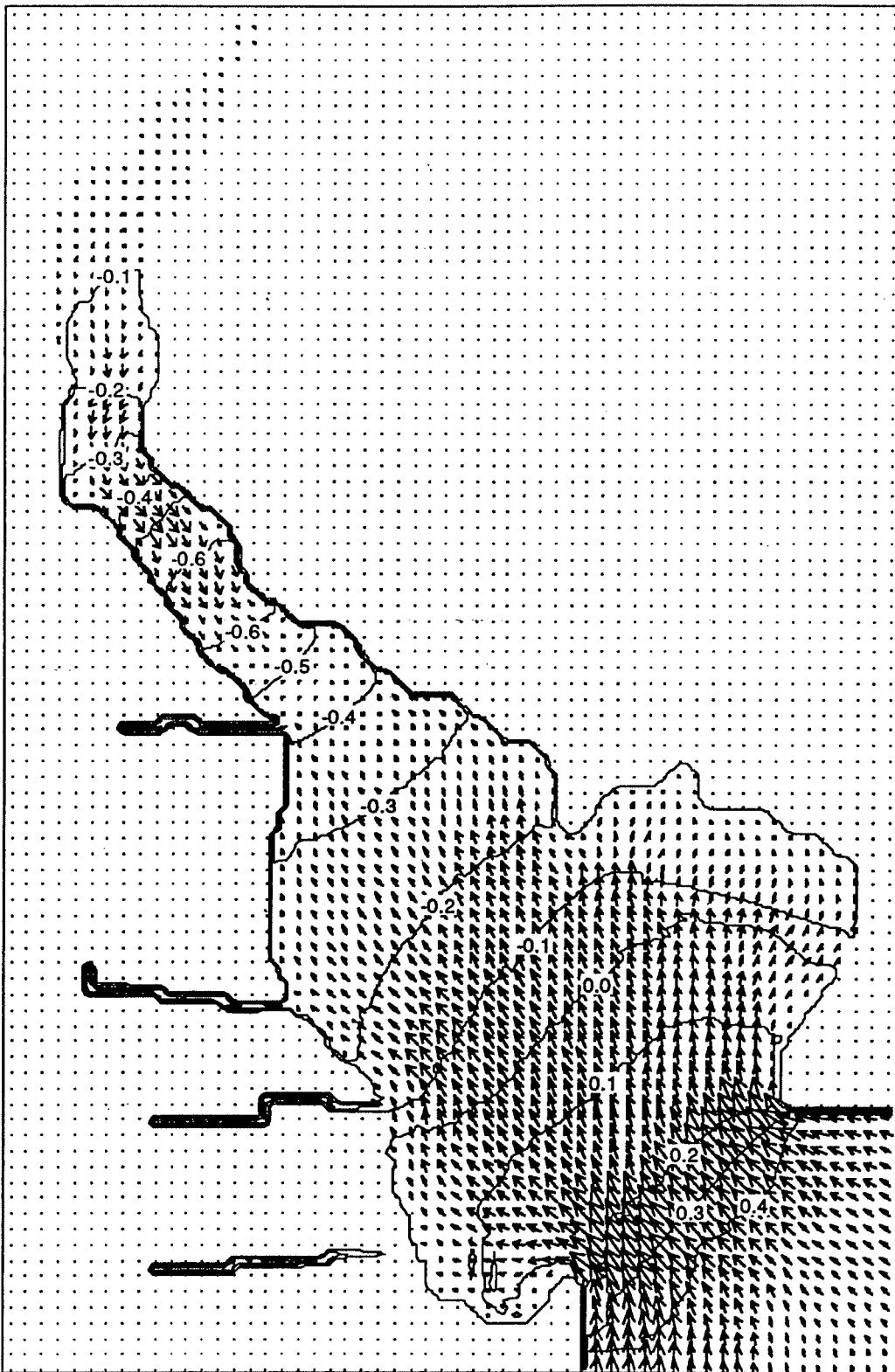


Fig. 5.1.3: Computed flow distribution 14 hours into simulation. Sea surface elevations are departures (m) from mean level.

UNCLASSIFIED

UNCLASSIFIED

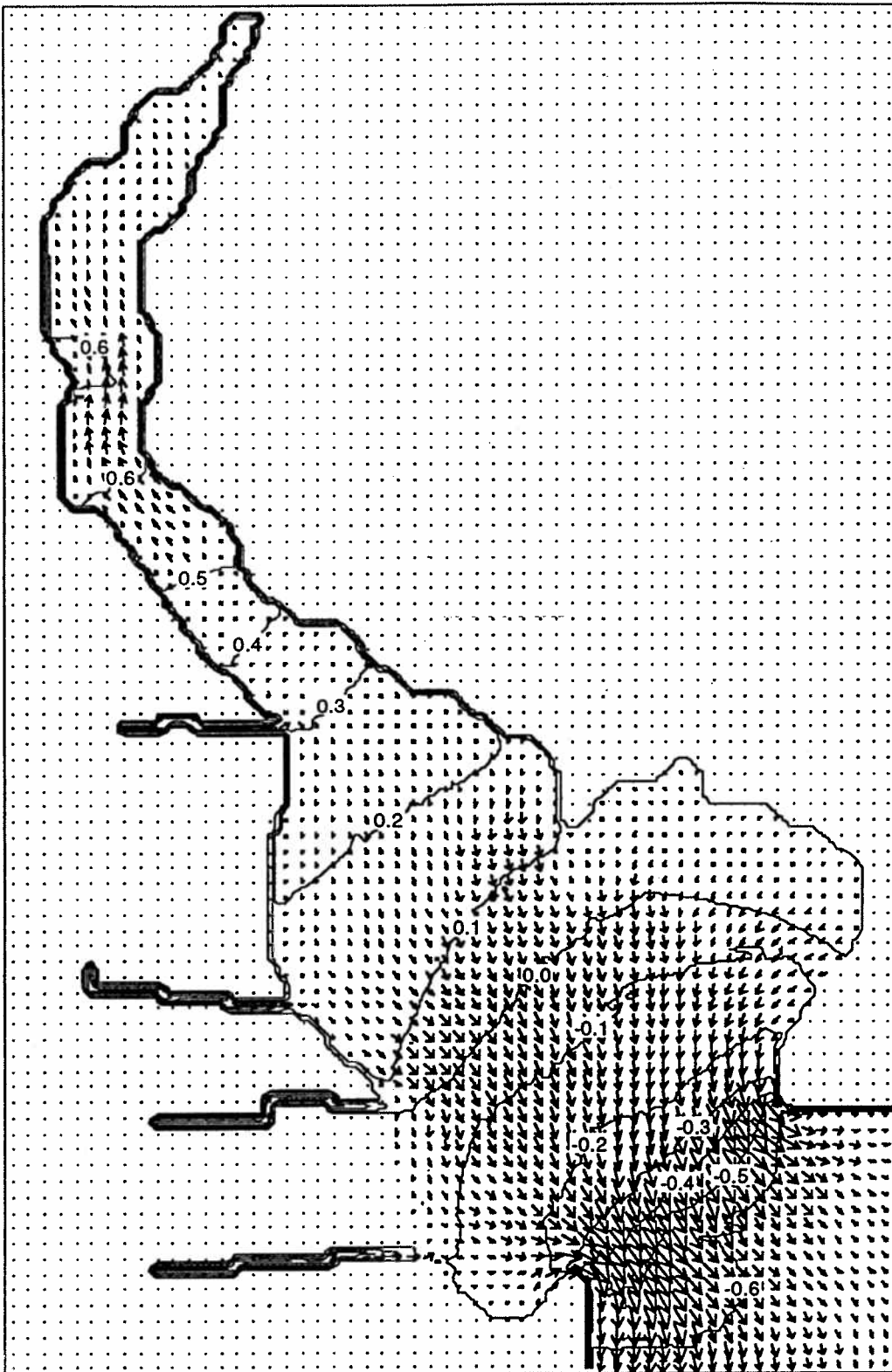


Fig. 5.1.4: Computed flow distribution 20 hours into simulation. Sea surface elevations are departures (m) from mean level.

UNCLASSIFIED

UNCLASSIFIED

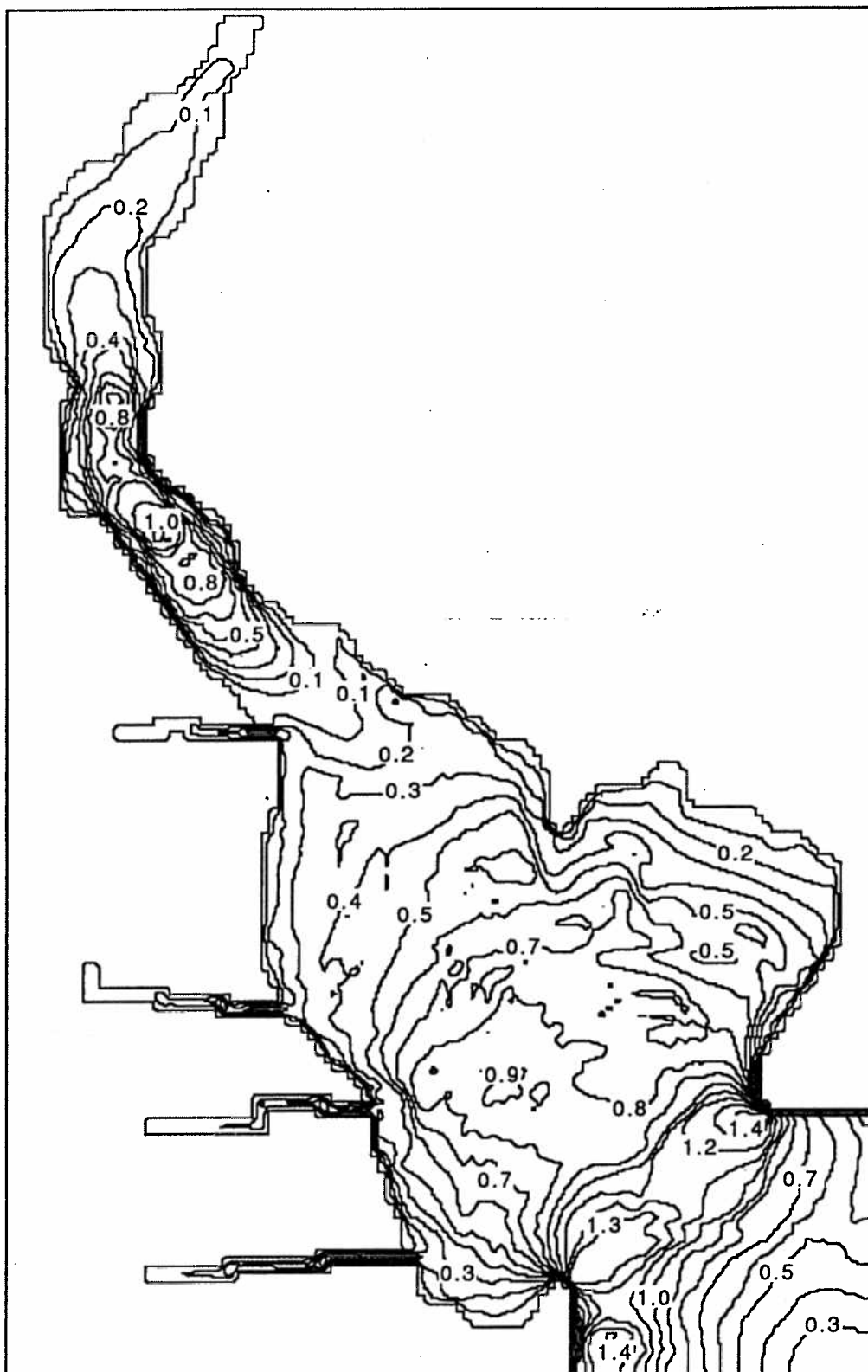


Fig. 5.1.5: Flood tide maximum current speeds (m/s) corresponding to velocity distribution in Fig. 5.1.3.

UNCLASSIFIED

UNCLASSIFIED

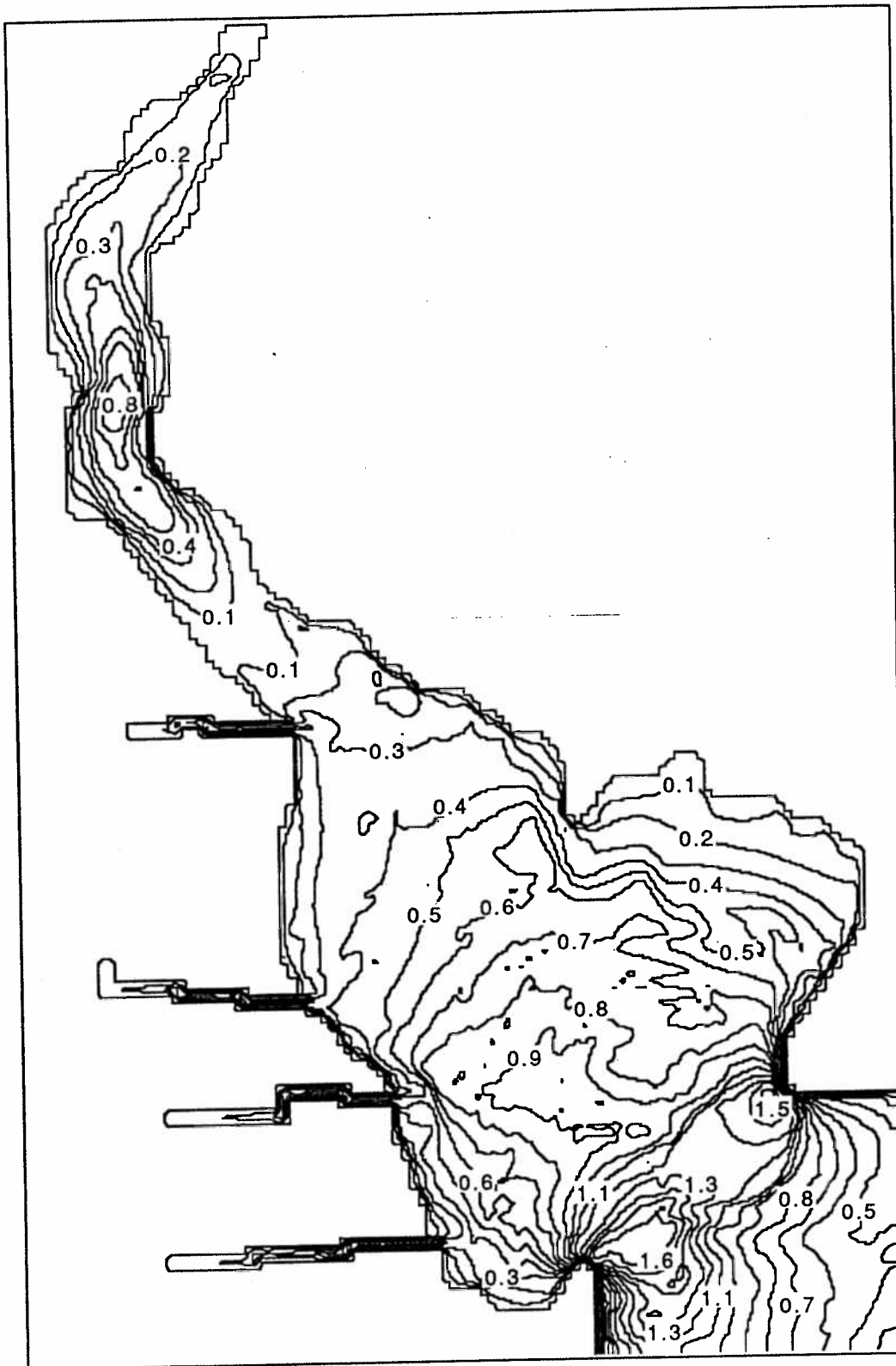
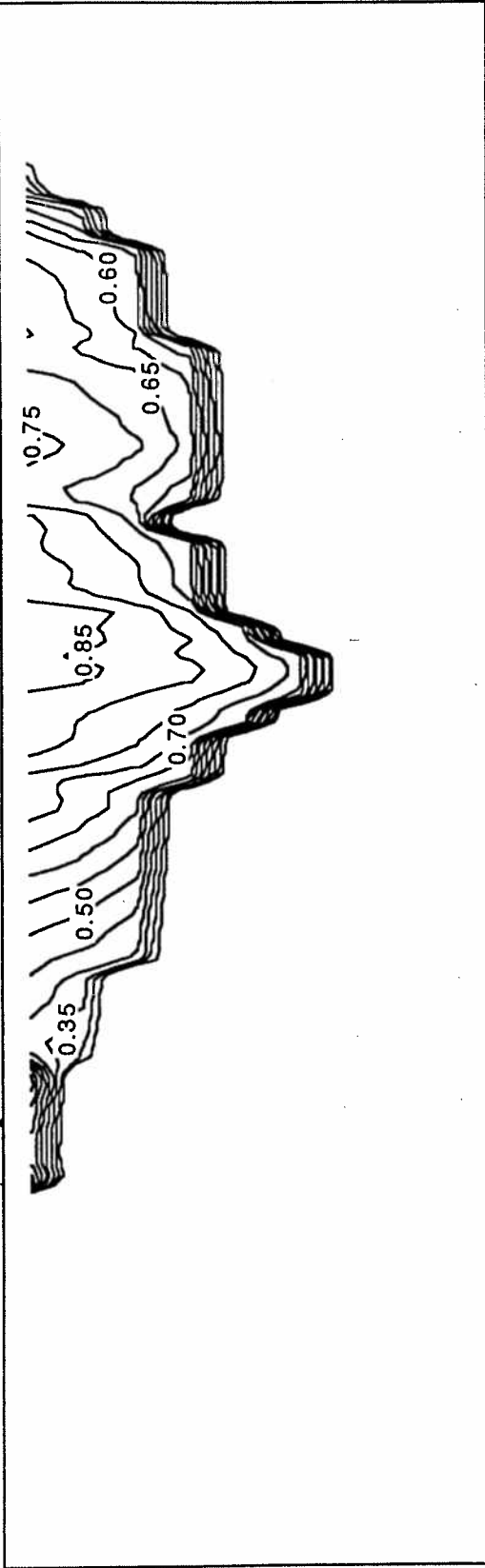


Fig. 5.1.6: Ebb tide maximum current speeds (m/s) corresponding to velocity distribution in Fig. 5.1.4.

UNCLASSIFIED

UNCLASSIFIED

Current speeds 10 km inland from mouth of Delaware Bay



Current speeds at mouth of Delaware Bay

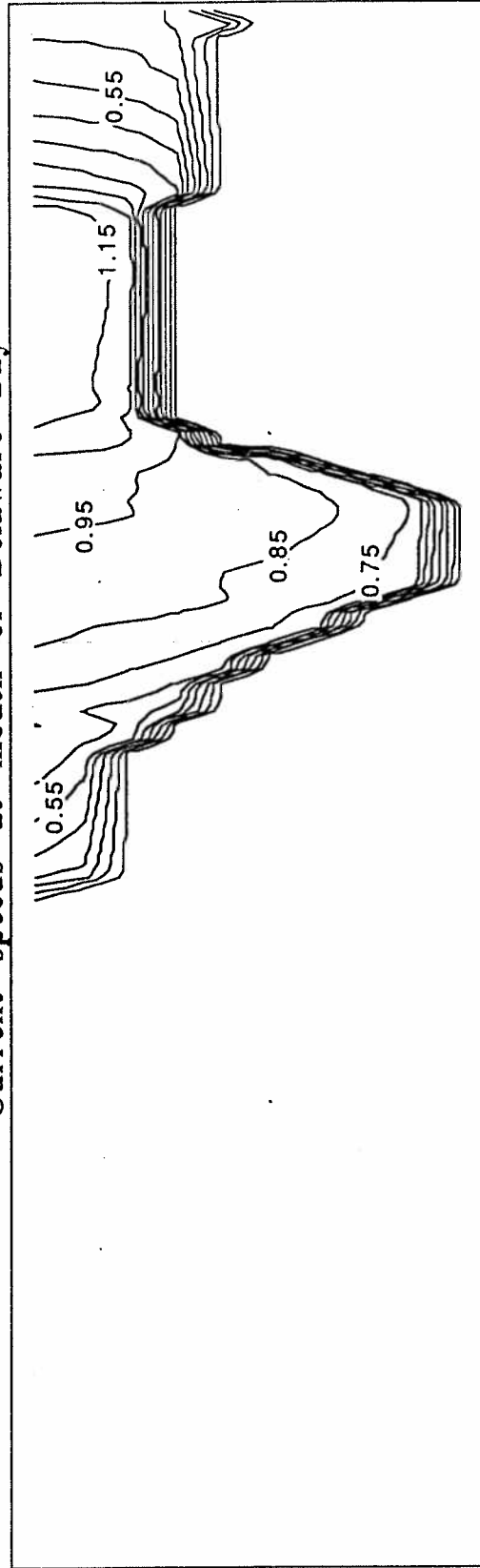
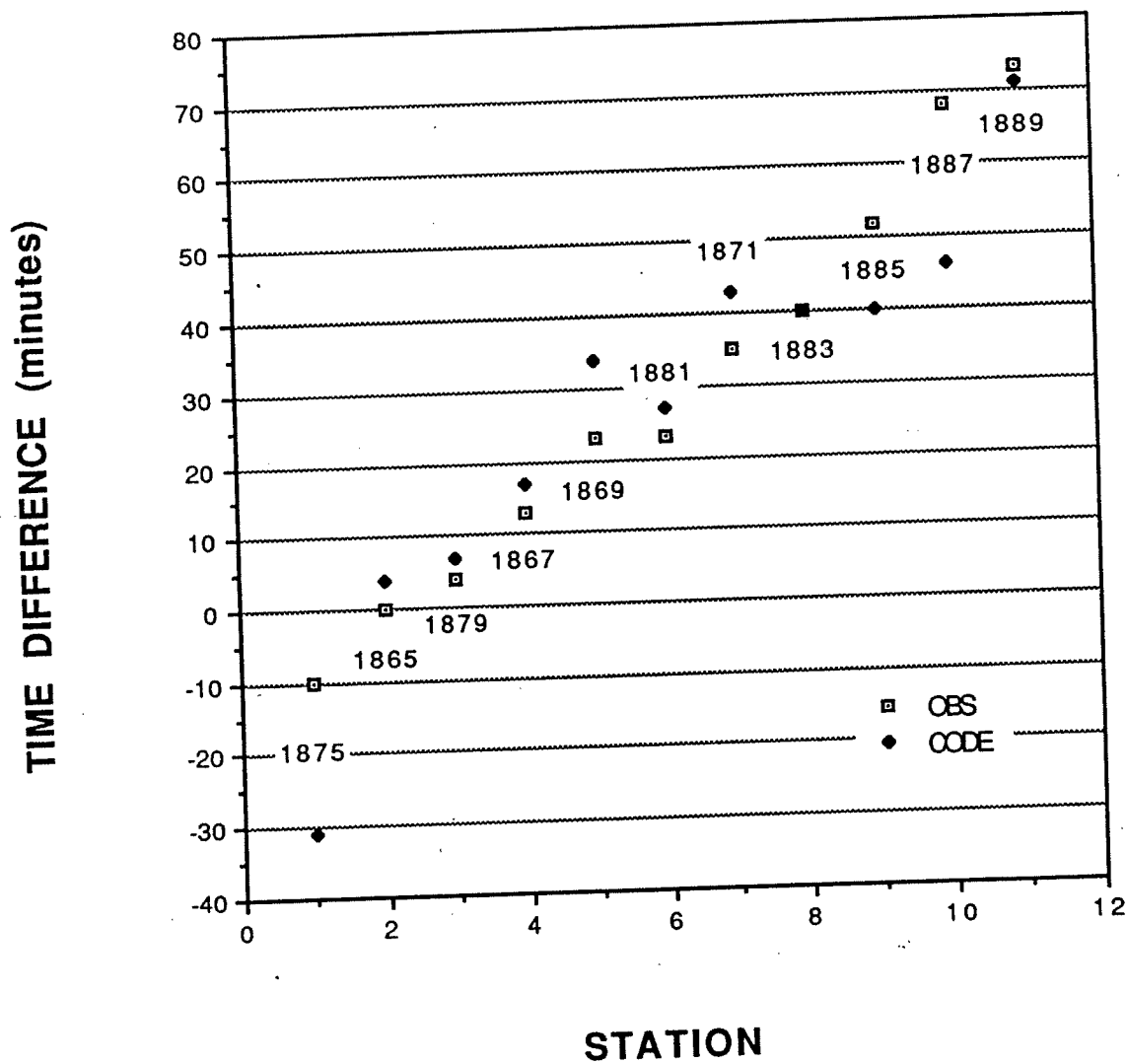


Fig. 5.1.7: Vertical crosssections of current speeds (m/s) at mouth of Delaware Bay and about 10 km in from the mouth.

UNCLASSIFIED

UNCLASSIFIED

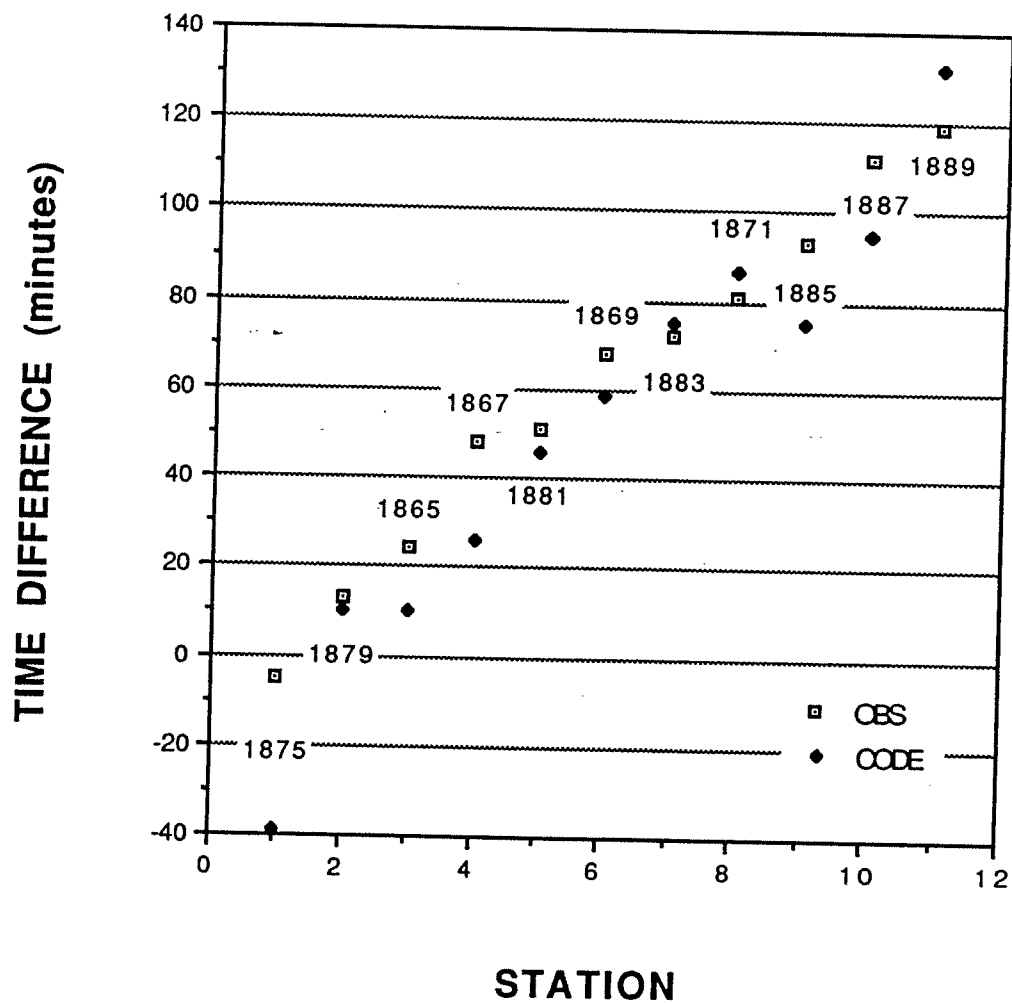
Fig. 5.1.8: Observed and computed lag times of high tide in Delaware Bay referenced to NOAA Station 1877



UNCLASSIFIED

UNCLASSIFIED

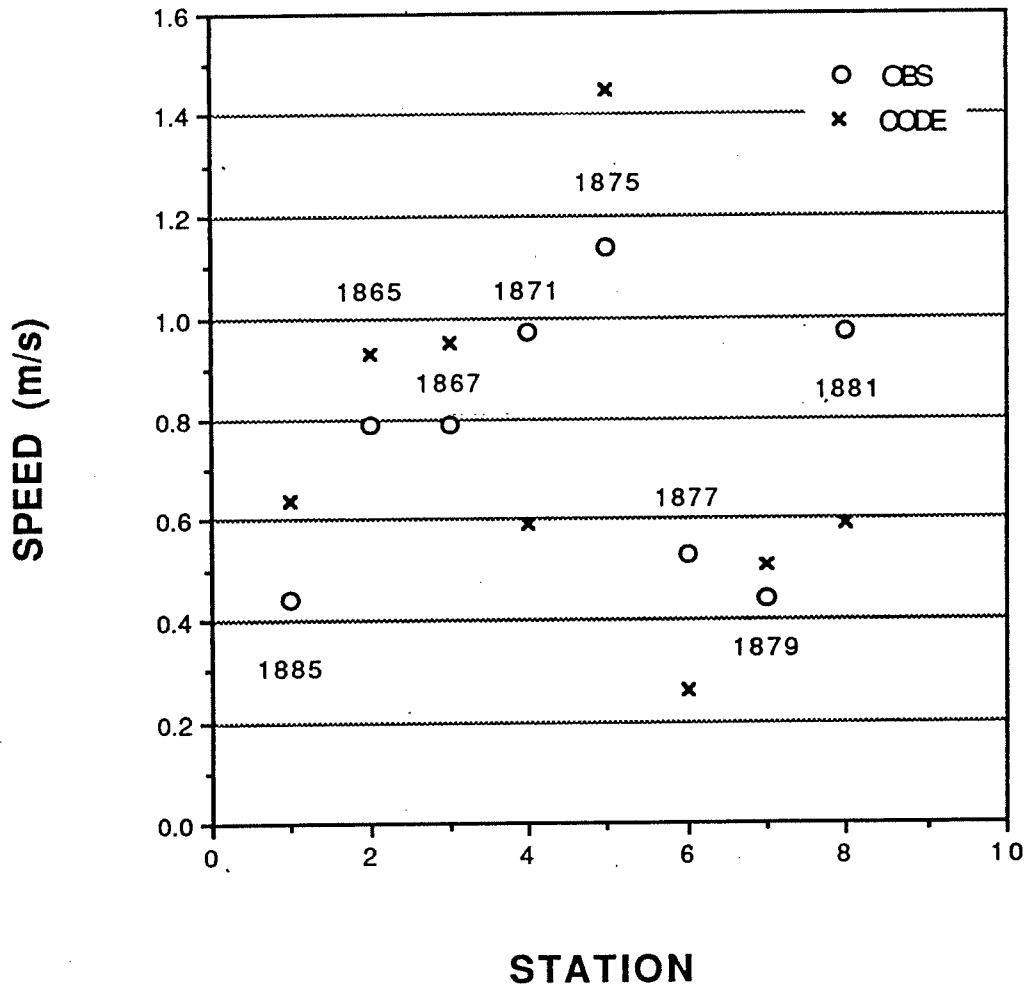
Fig. 5.1.9: Observed and computed lag times of low tide in Delaware Bay referenced to NOAA Station 1877



UNCLASSIFIED

UNCLASSIFIED

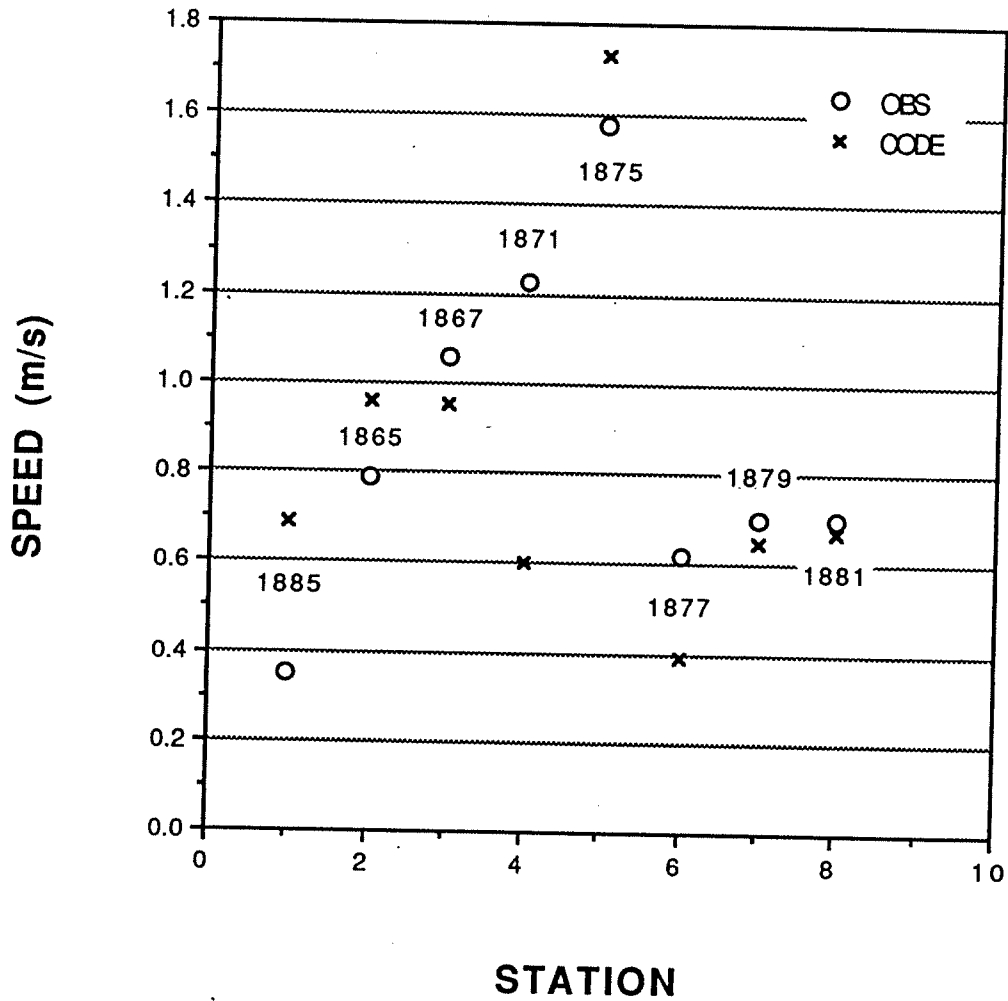
Fig. 5.1.10: Observed and computed maximum current speeds in Delaware Bay during incoming (flooding) tide



UNCLASSIFIED

UNCLASSIFIED

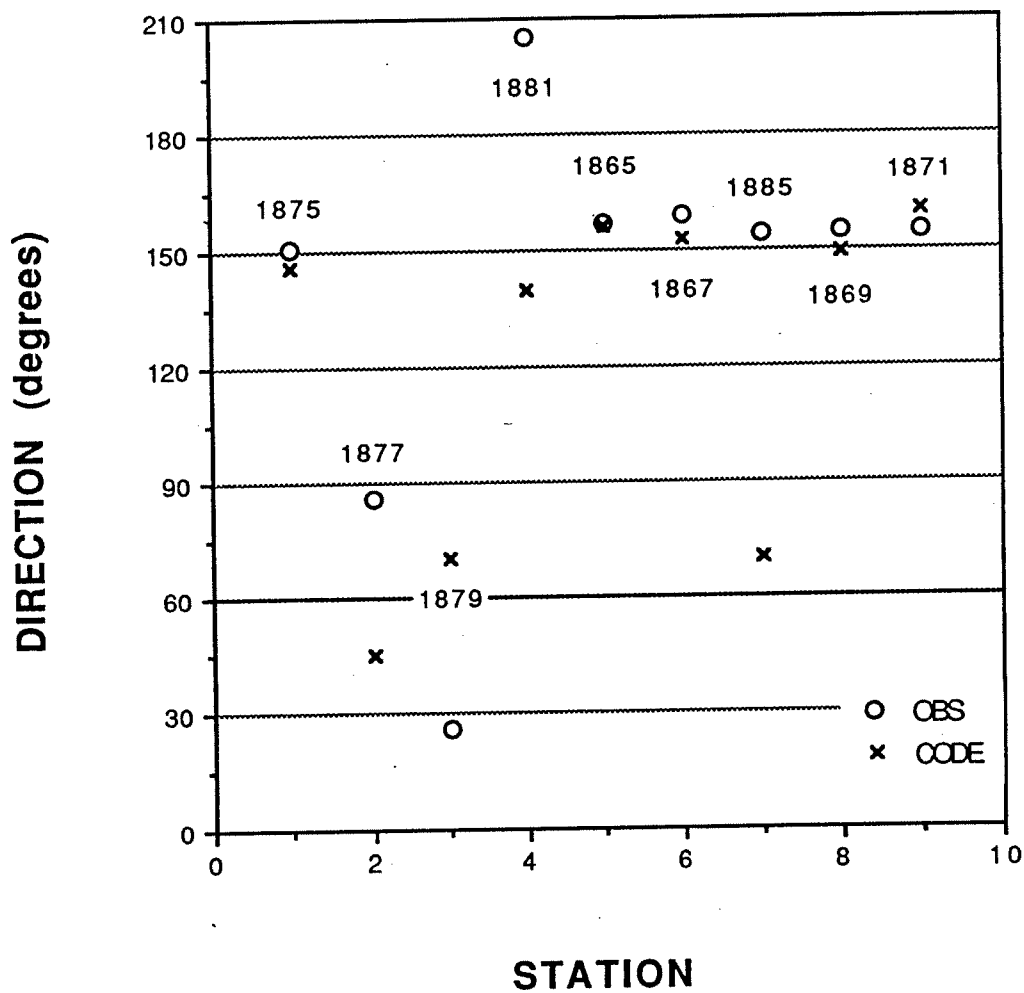
Fig. 5.1.11: Observed and computed maximum current speeds in Delaware Bay during outgoing (ebbing) tide



UNCLASSIFIED

UNCLASSIFIED

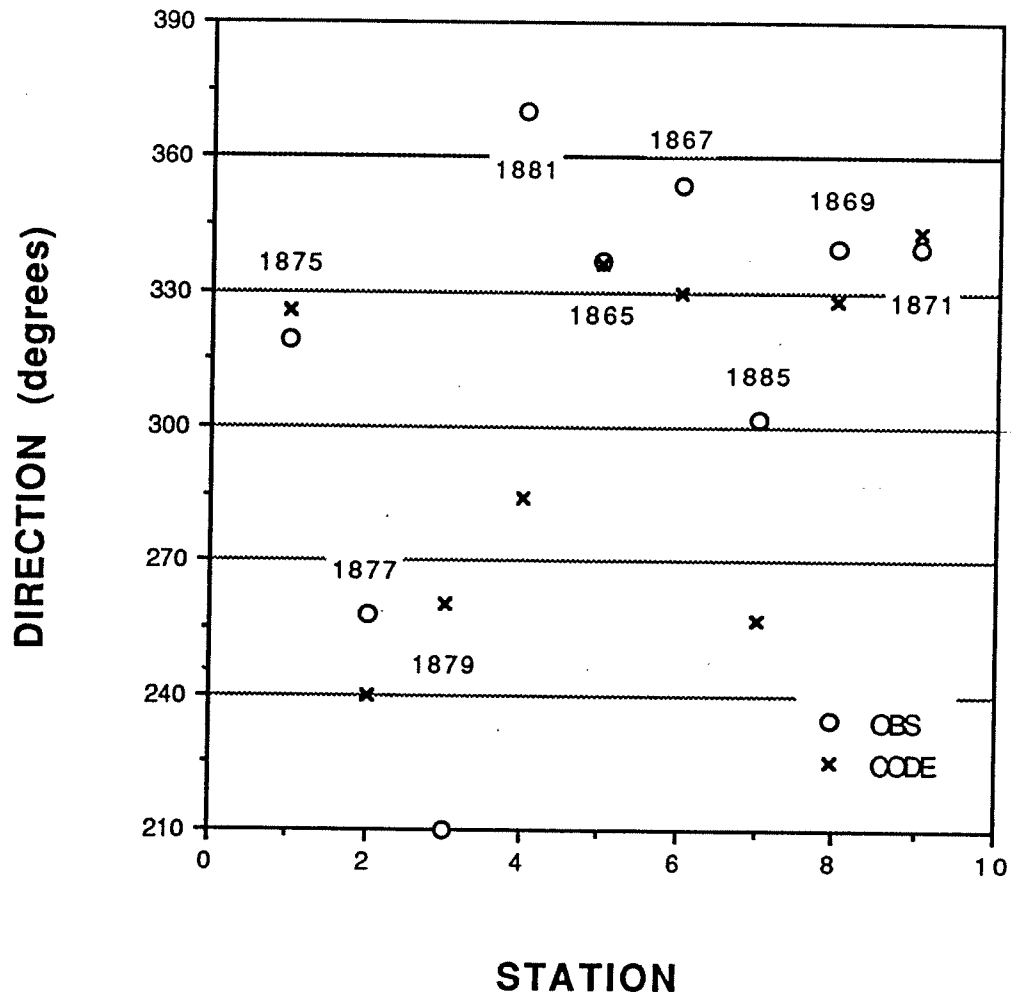
Fig. 5.1.12: Observed and computed current directions in Delaware Bay during incoming (flooding) tide



UNCLASSIFIED

UNCLASSIFIED

Fig. 5.1.13: Observed and computed current directions in Delaware Bay during outgoing (ebbing) tide



UNCLASSIFIED

UNCLASSIFIED

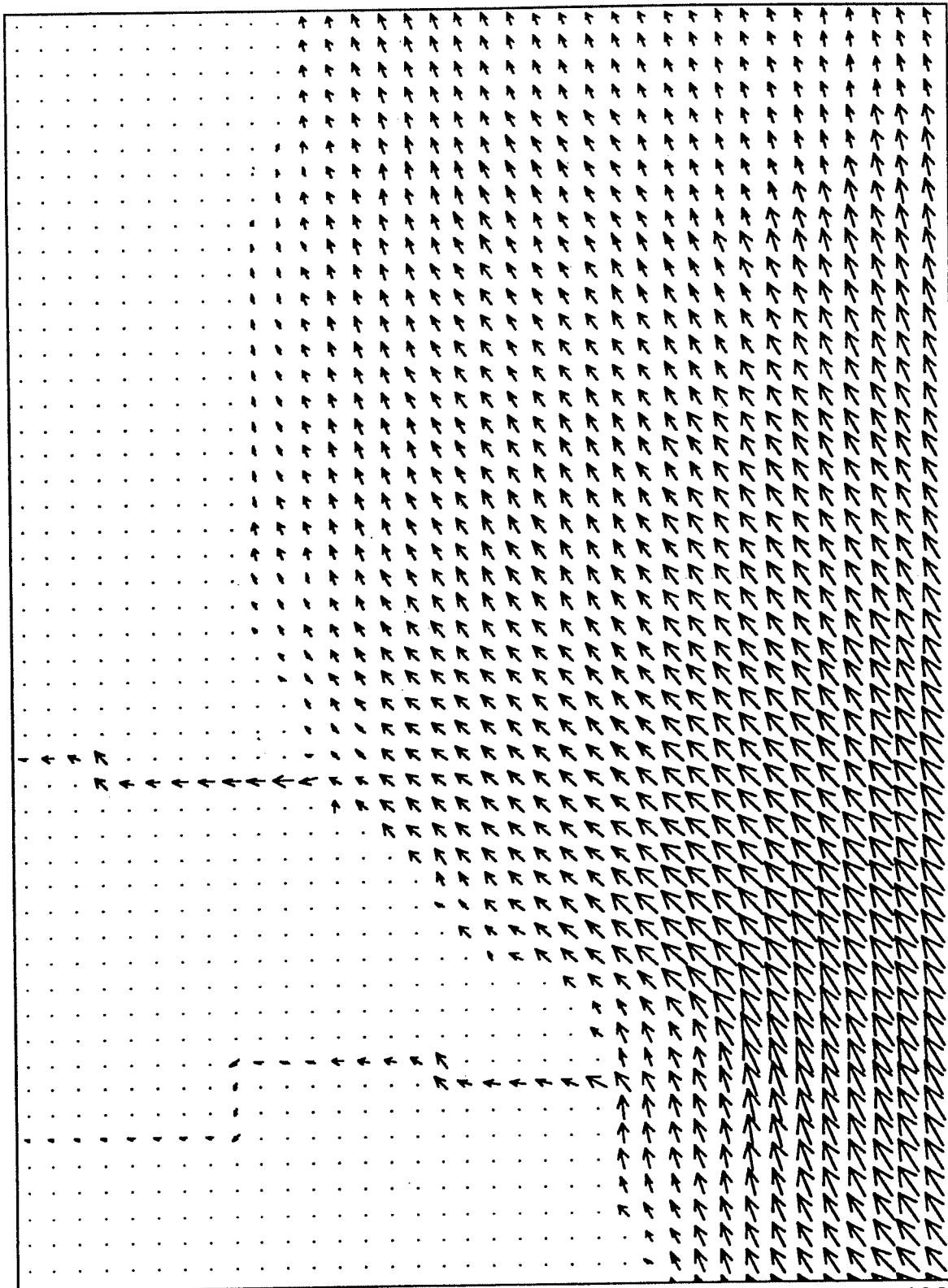


Fig. 5.1.14: Surface flow field near stations 1881 and 1885 illustrating rapid change in flow direction near inlets to tidal creeks during flooding tide.

UNCLASSIFIED

UNCLASSIFIED

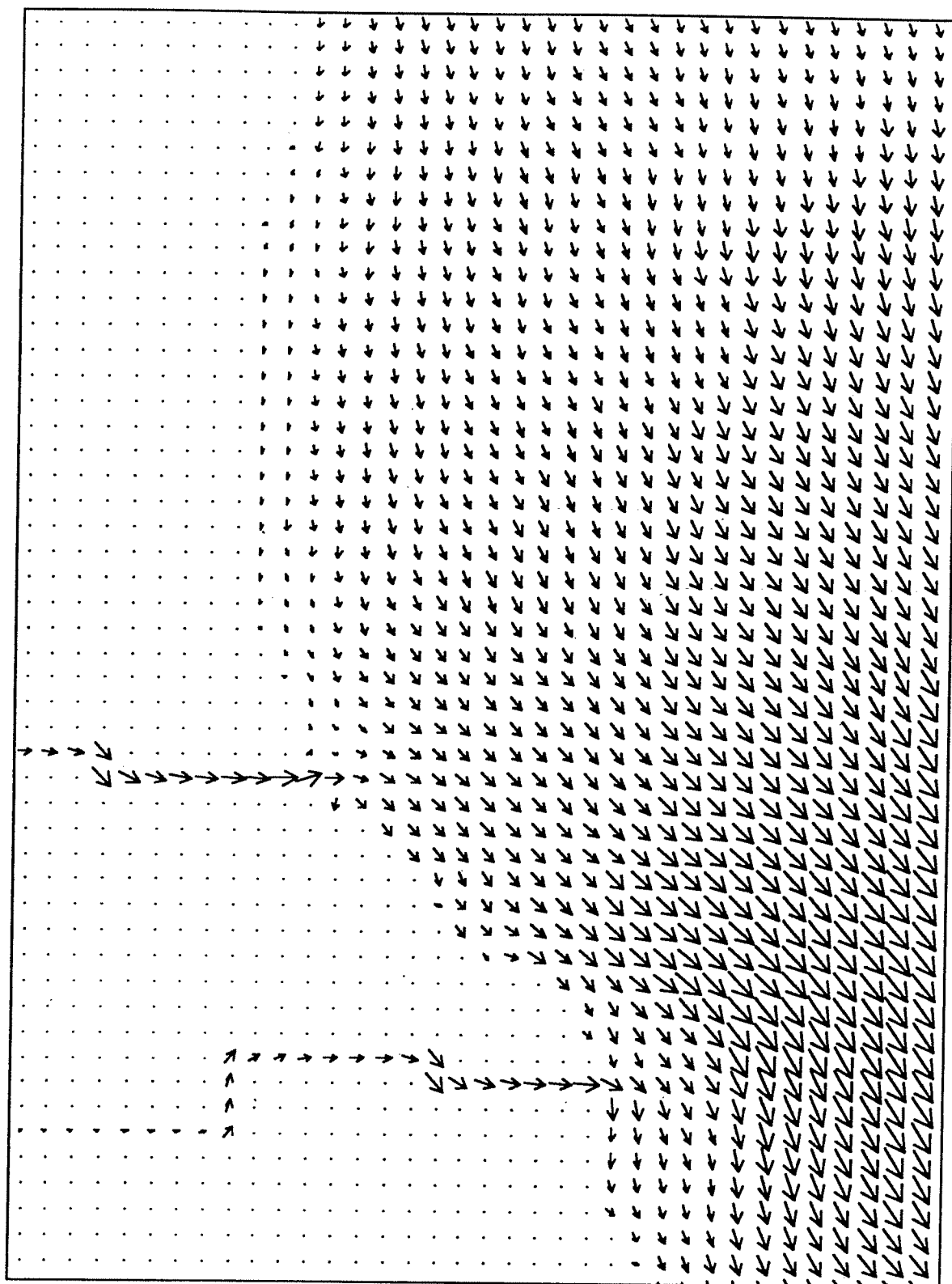
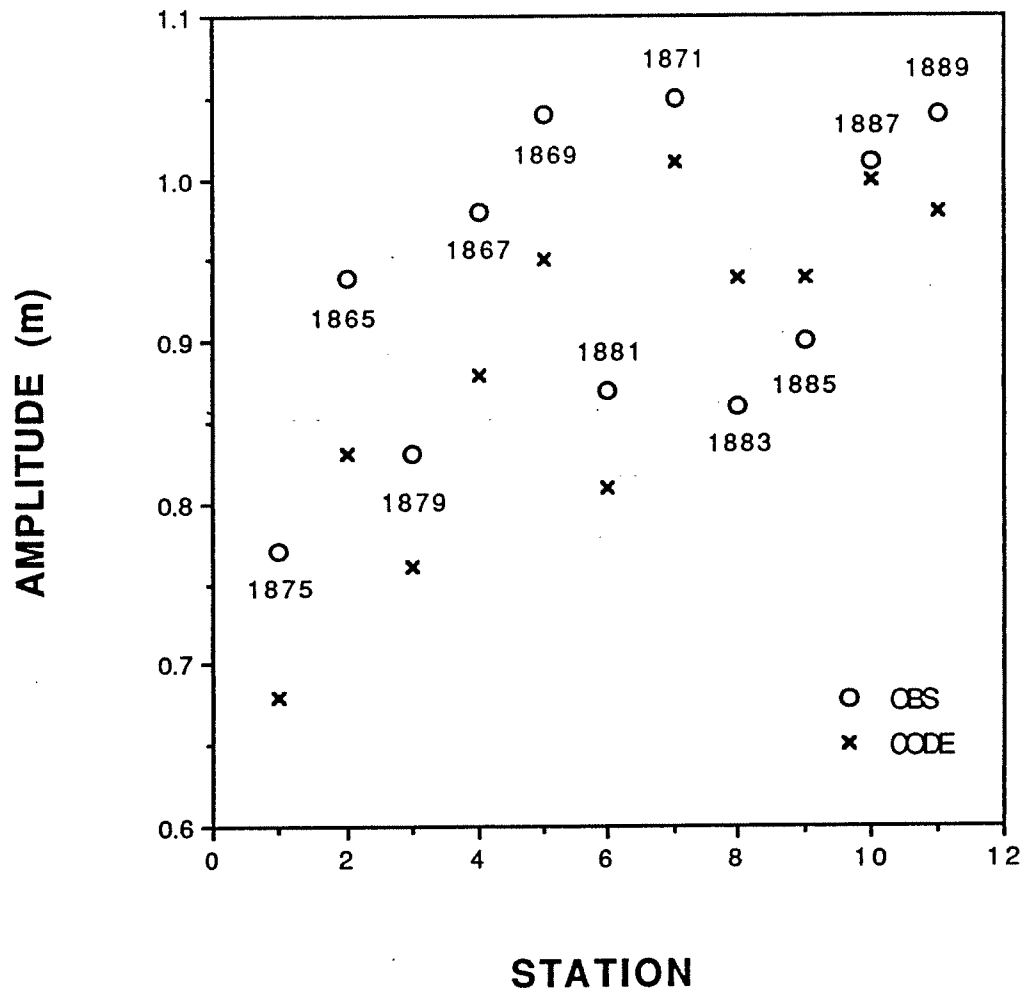


Fig. 5.1.15: Surface flow field near stations 1881 and 1885 illustrating rapid change in flow direction near inlets to tidal creeks during ebbing tide.

UNCLASSIFIED

UNCLASSIFIED

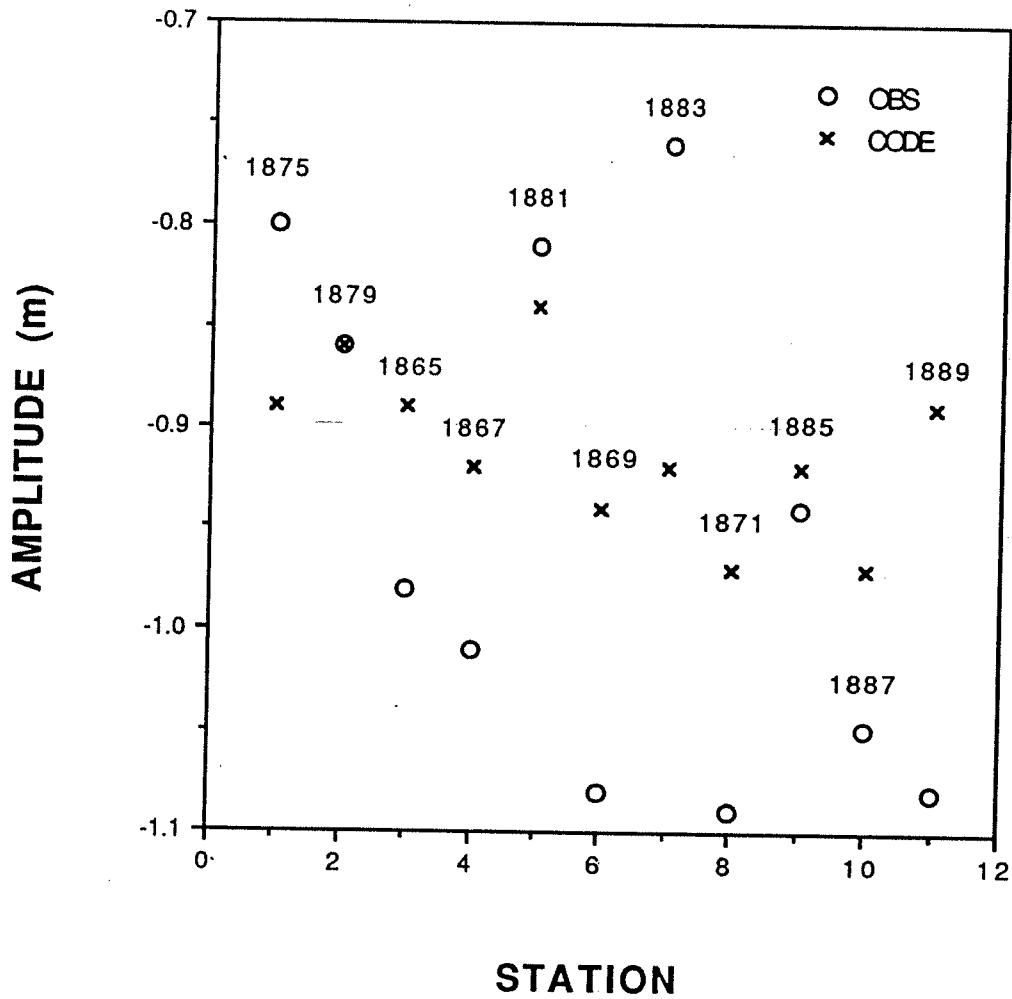
Fig. 5.1.16: Observed and computed high tide amplitudes in Delaware Bay



UNCLASSIFIED

UNCLASSIFIED

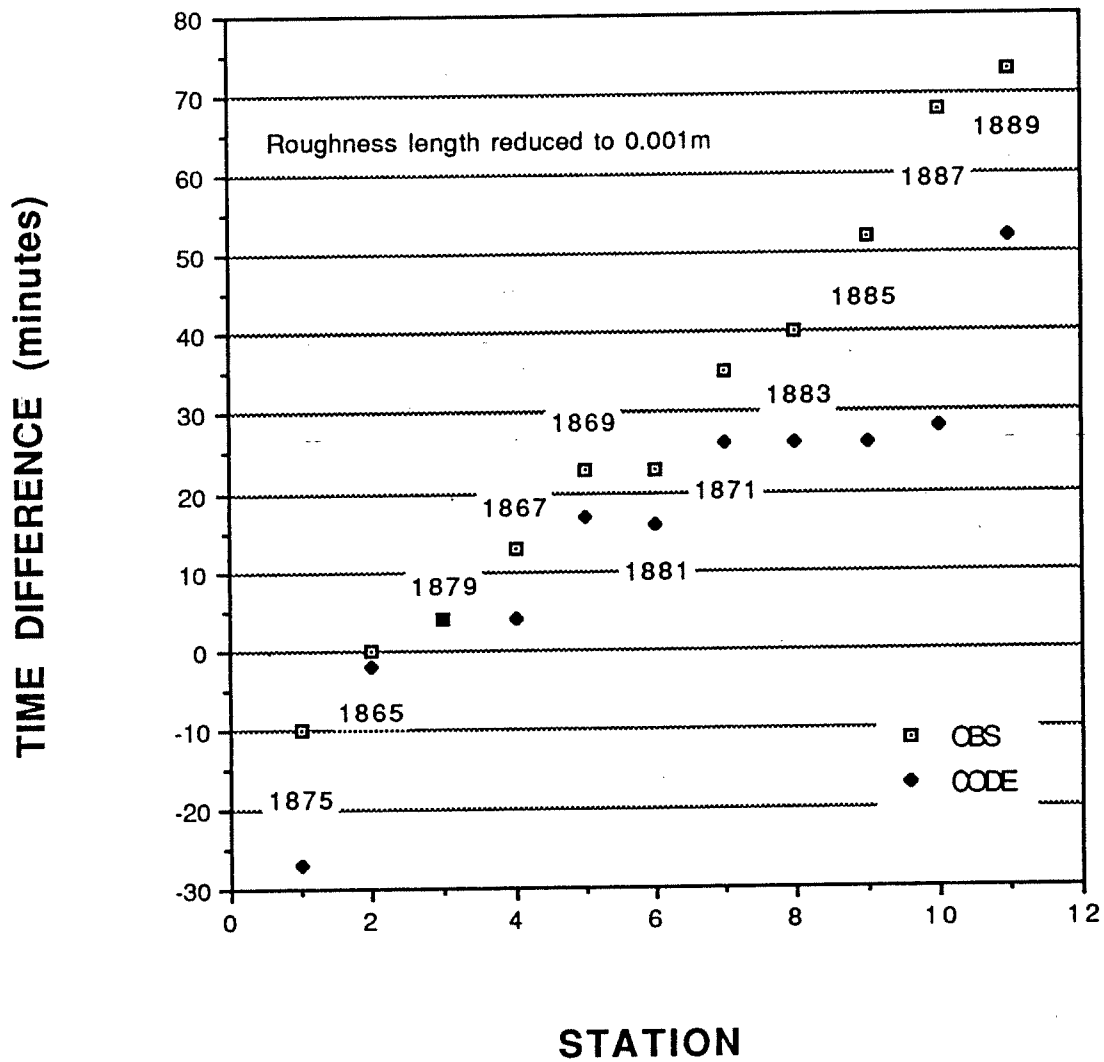
Fig. 5.1.17: Observed and computed low tide amplitudes in Delaware Bay



UNCLASSIFIED

UNCLASSIFIED

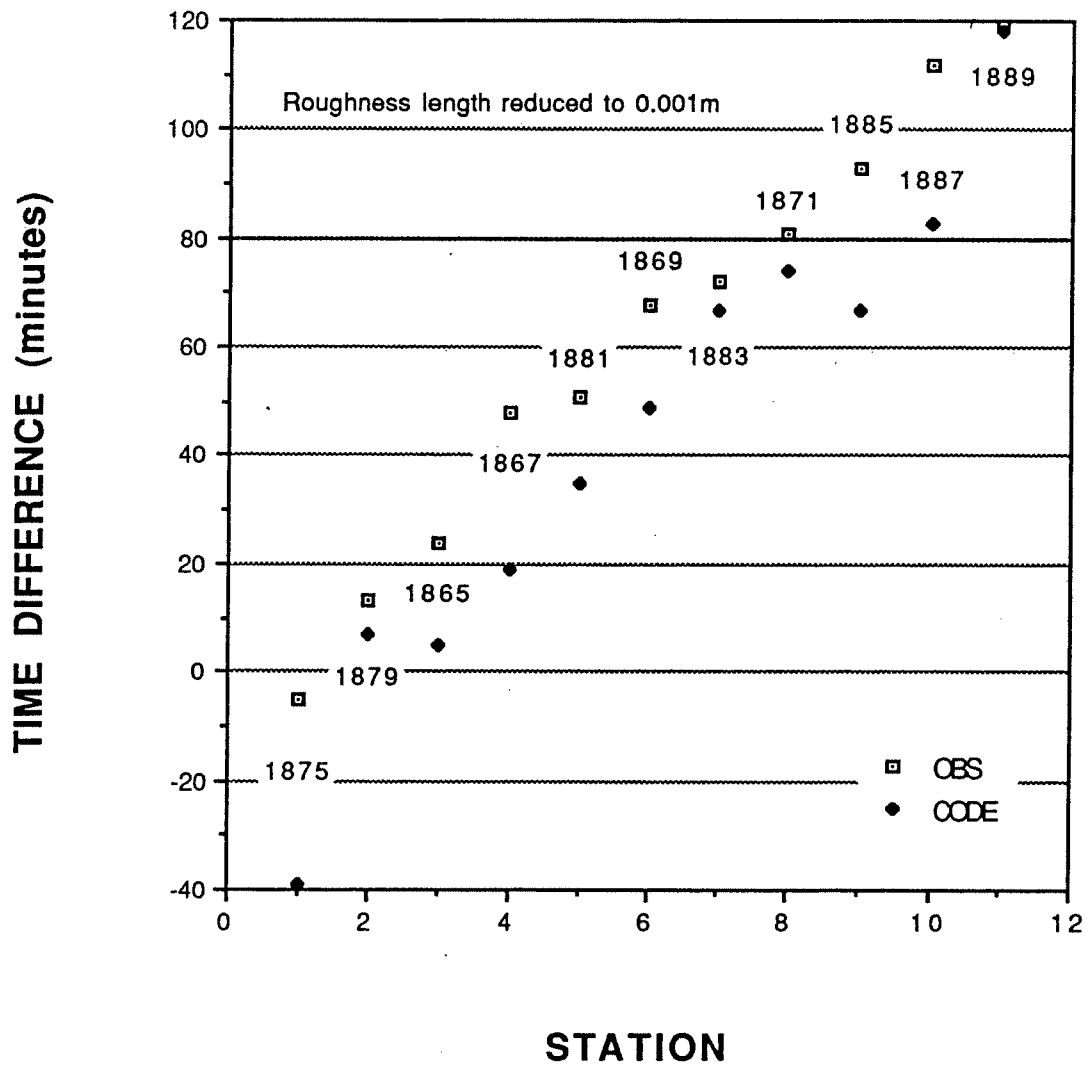
Fig. 5.1.18: Observed and computed lag times of high tide in Delaware Bay referenced to NOAA Station 1877.



UNCLASSIFIED

UNCLASSIFIED

Fig. 5.1.19: Observed and computed lag times of low tide in Delaware Bay referenced to NOAA Station 1877



UNCLASSIFIED

UNCLASSIFIED

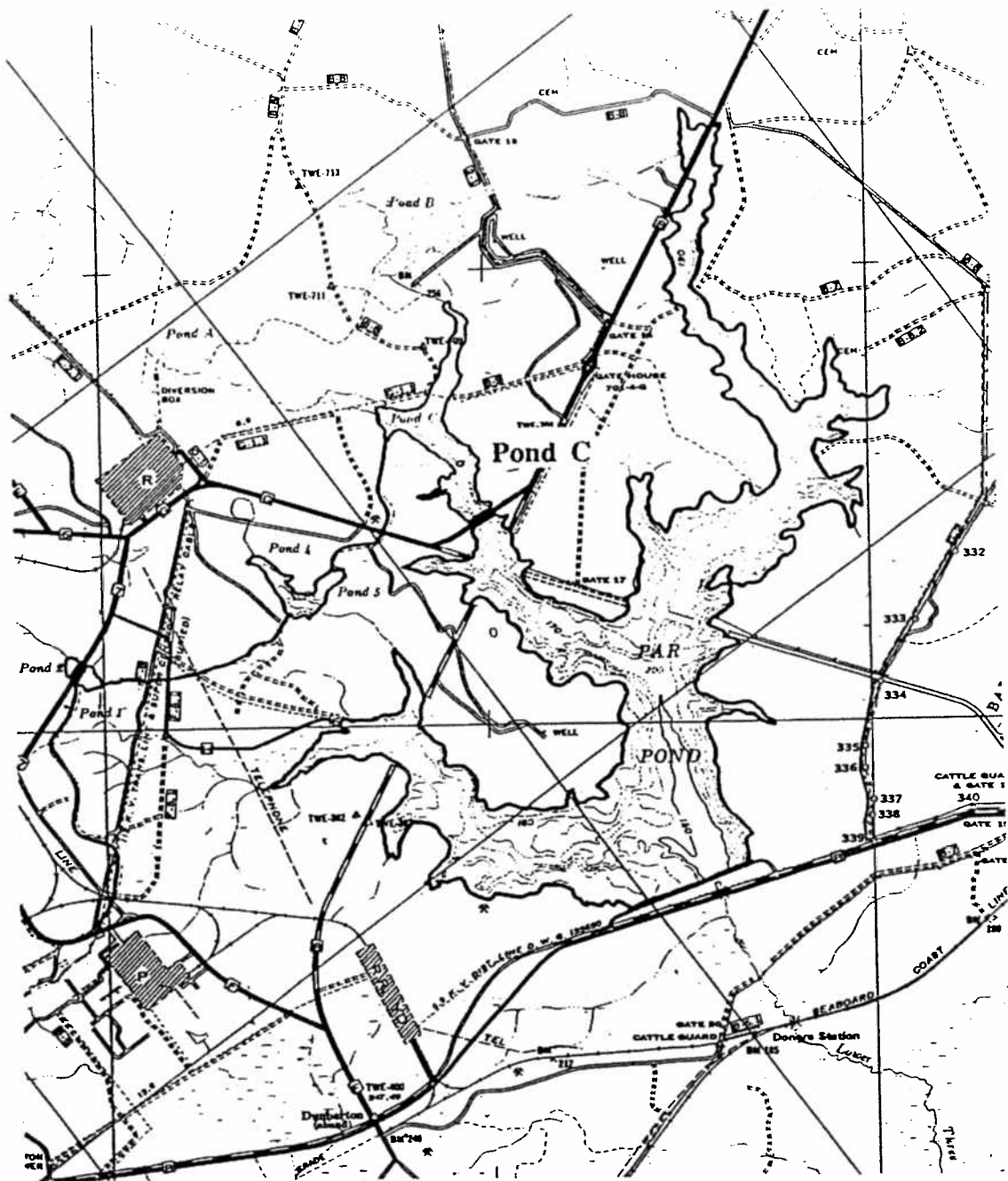


Fig. 5.2.1: Location of SRS Pond C relative to P Reactor and Par Pond

UNCLASSIFIED

UNCLASSIFIED

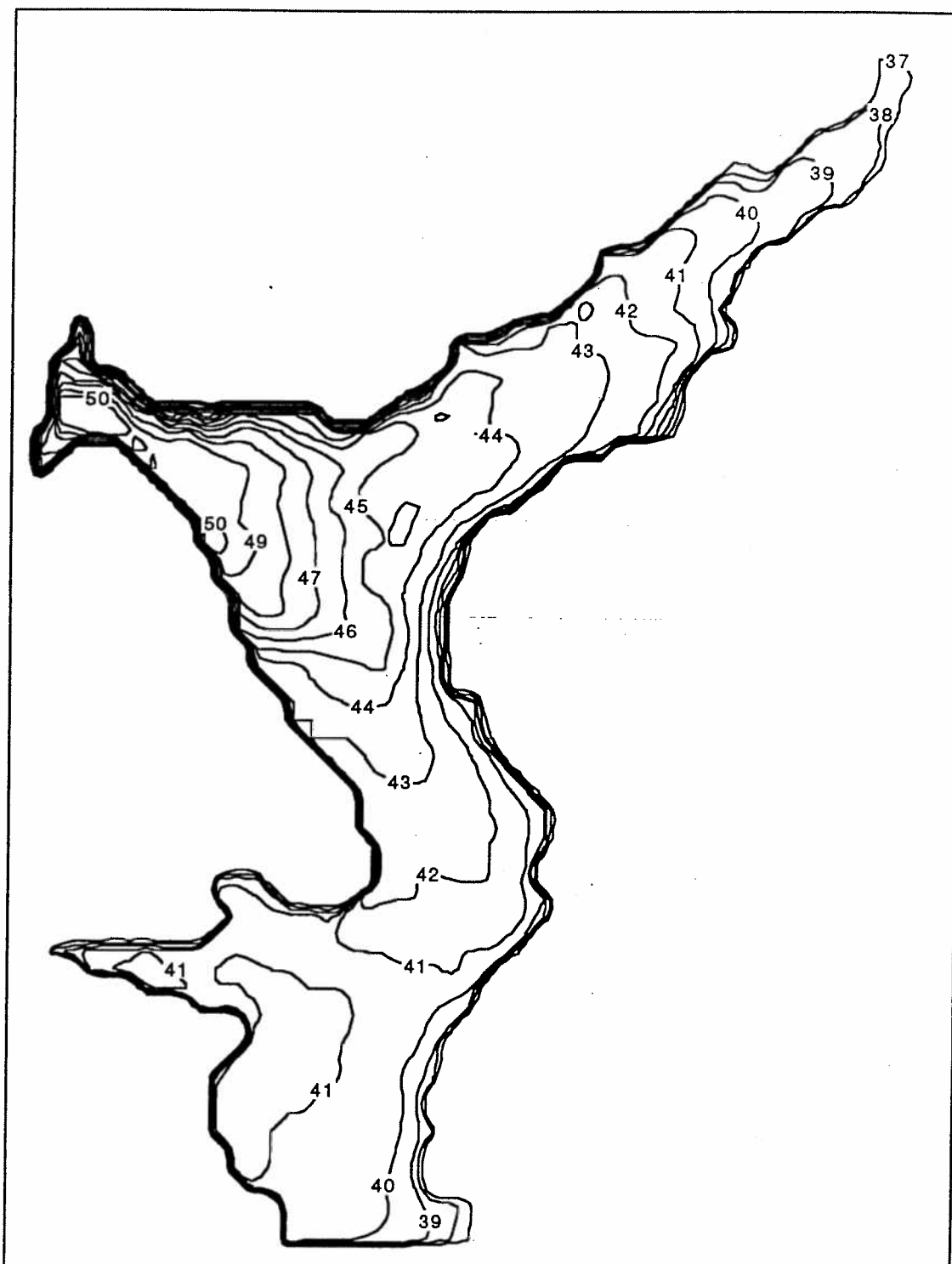


Fig. 5.2.2: Observed temperatures ($^{\circ}\text{C}$) in Pond C on April 2, 1984 at about noon local time.

UNCLASSIFIED

UNCLASSIFIED

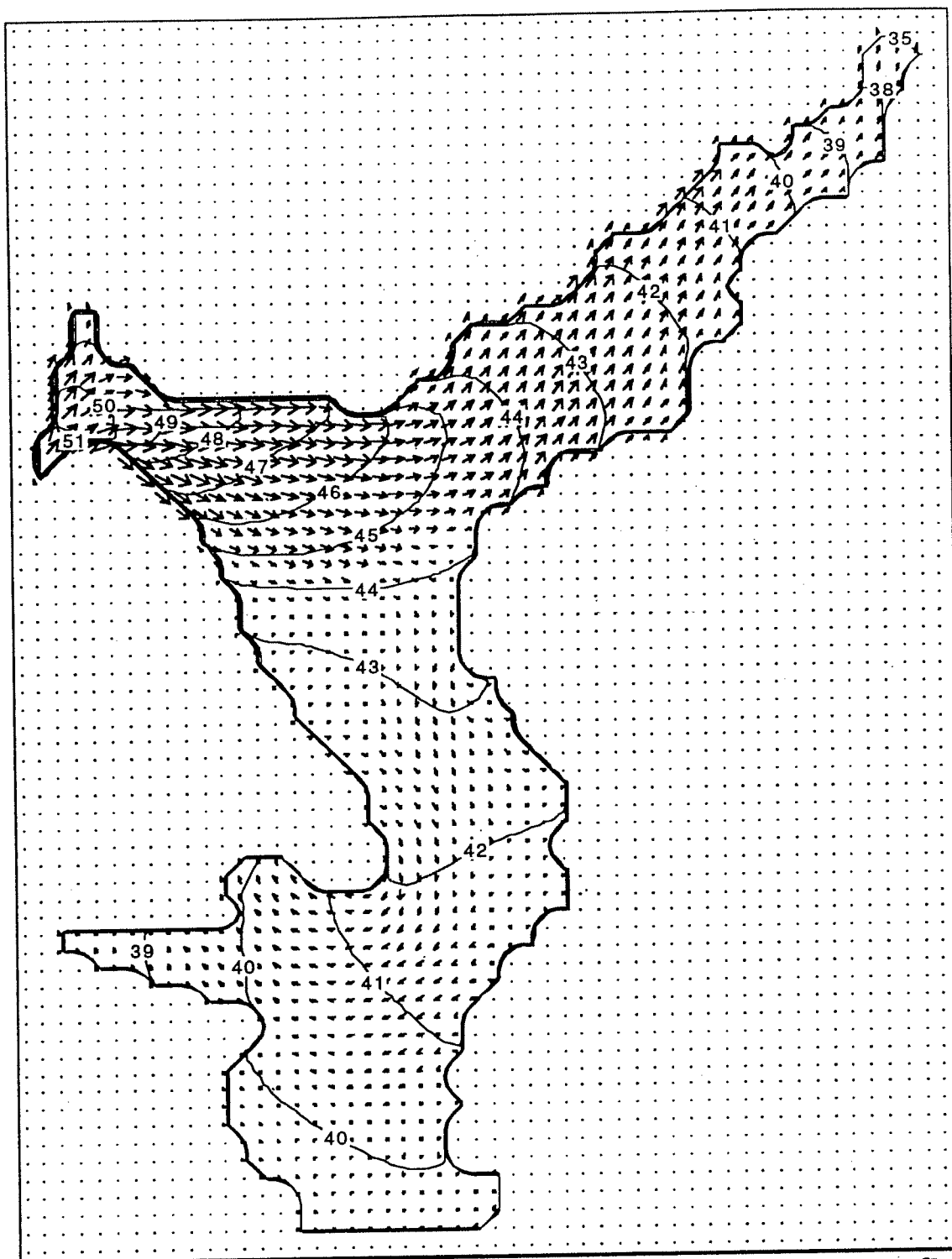


Fig. 5.2.3: Computed temperature contours ($^{\circ}\text{C}$) and flow vectors for Pond C on April 2, 1984 at about noon. Maximum velocity is 0.17 m/s.

UNCLASSIFIED

UNCLASSIFIED

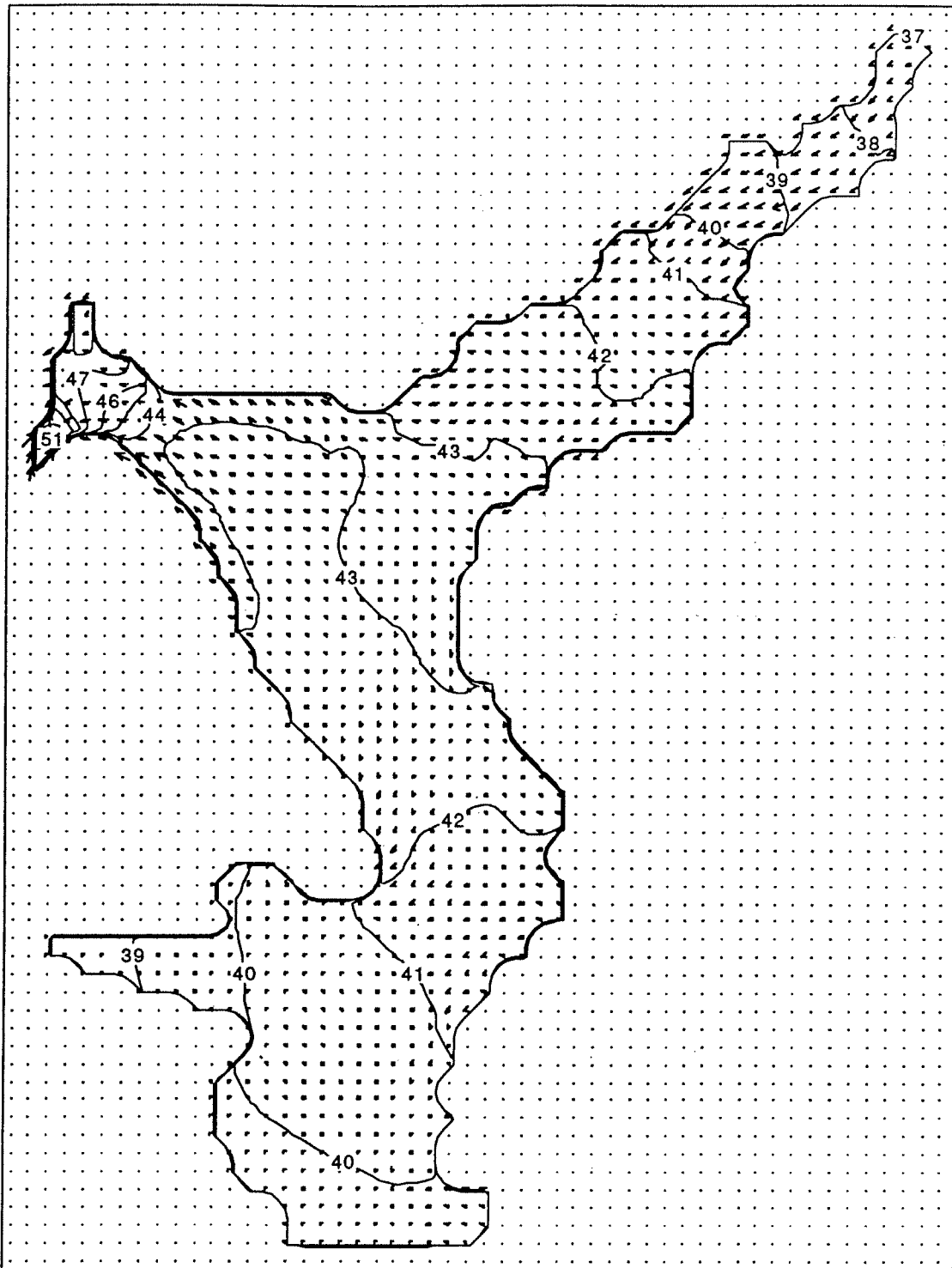


Fig. 5.2.4: Computed Pond C temperature contours ($^{\circ}\text{C}$) and flow vectors at a depth of 2 m. Note return flow from dead arm and in outfall arm. Maximum velocity is 0.14 m/s.

UNCLASSIFIED

UNCLASSIFIED

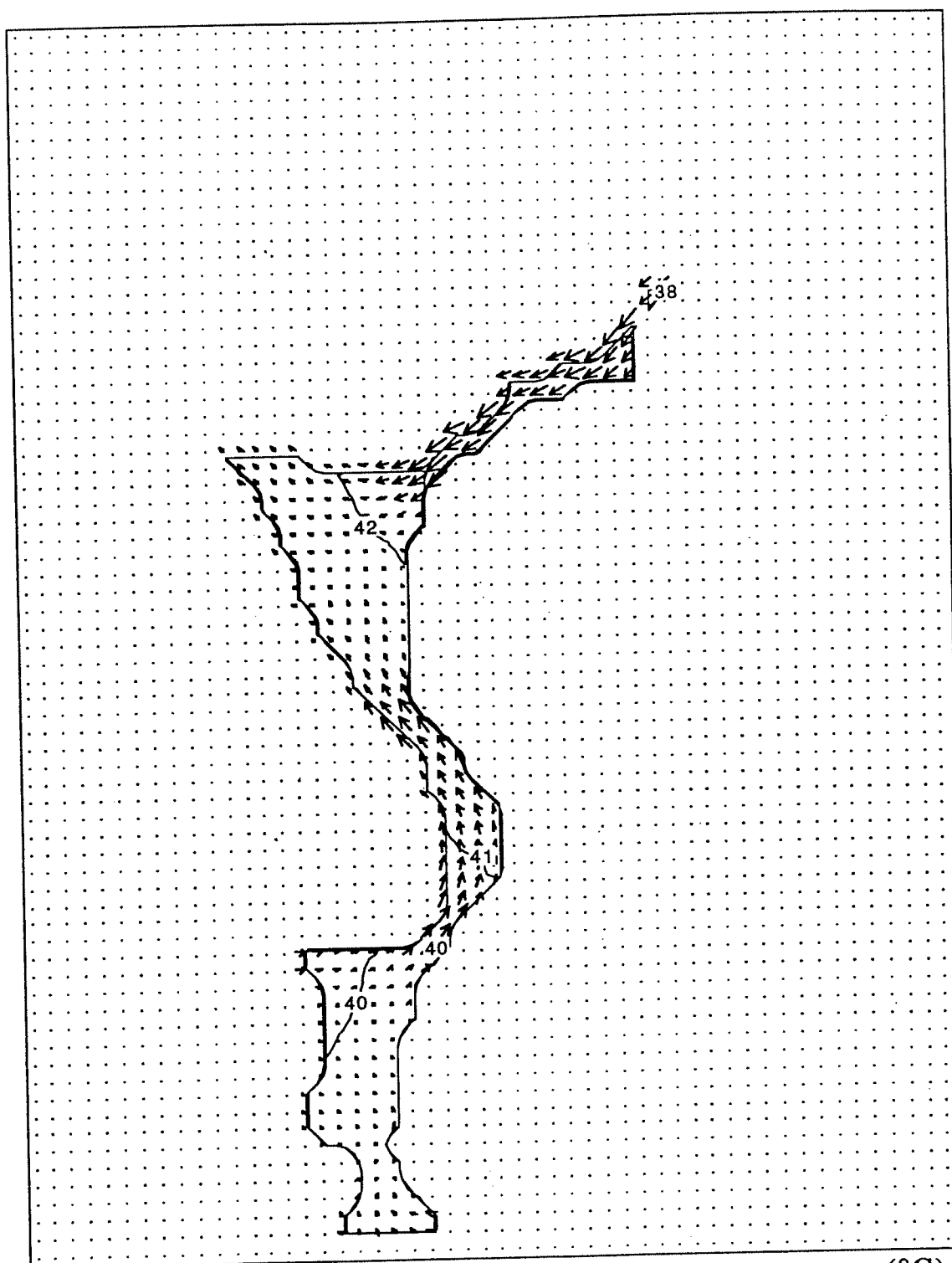


Fig. 5.2.5: Computed Pond C temperature contours ($^{\circ}\text{C}$) and flow vectors at a depth of 4 m. Note return flow from dead arm and from lower end of lake. Maximum velocity is 0.1 m/s.

UNCLASSIFIED

UNCLASSIFIED

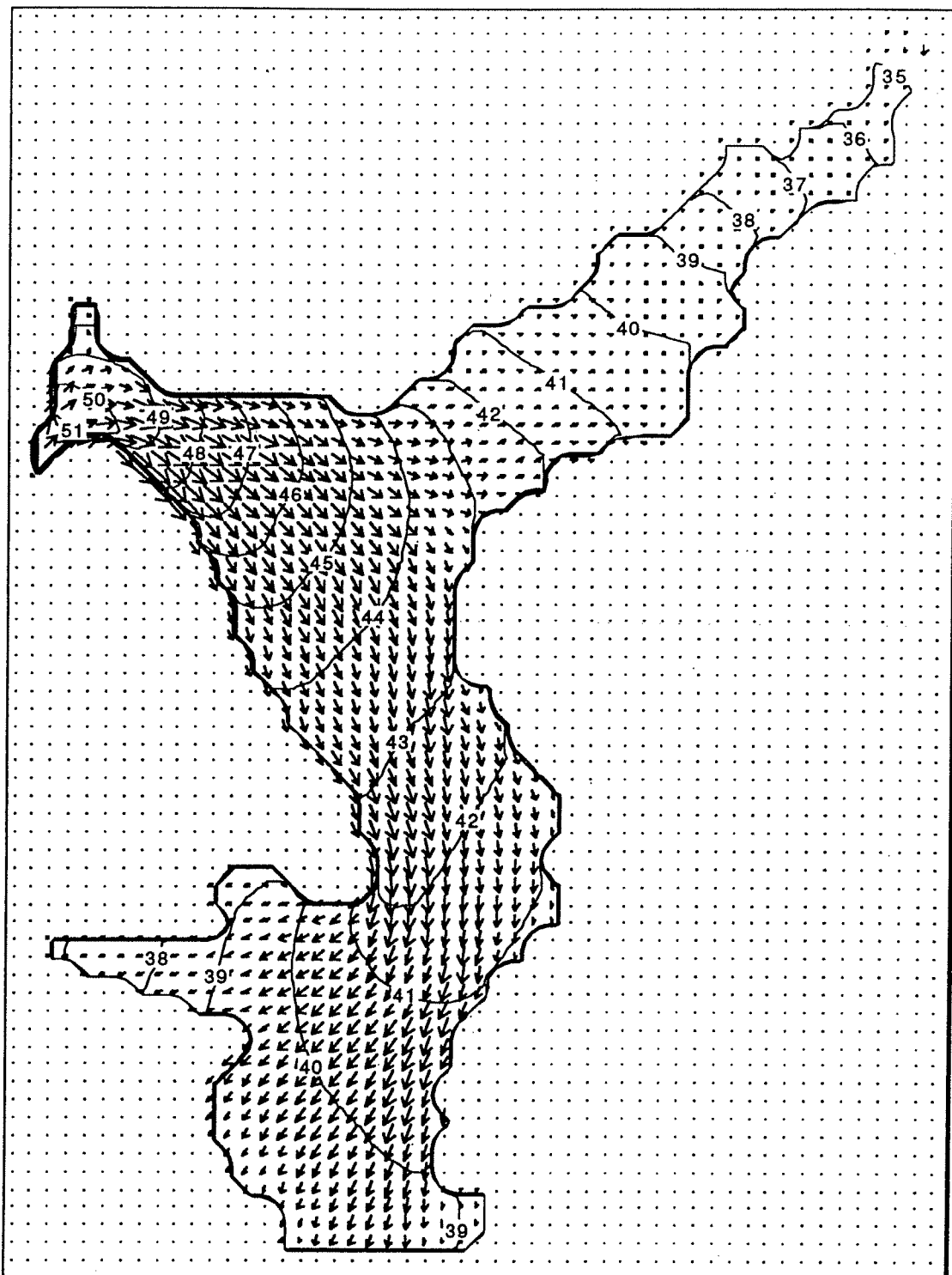


Fig. 5.2.6: Computed temperature contours ($^{\circ}\text{C}$) and flow vectors for Pond C on April 2, 1984 at about noon with wind from west-northwest. Maximum velocity is 0.16 m/s.

UNCLASSIFIED

UNCLASSIFIED



Fig. 5.3.1: Map of SRS L Lake. L Reactor location is at top of map.

UNCLASSIFIED

UNCLASSIFIED

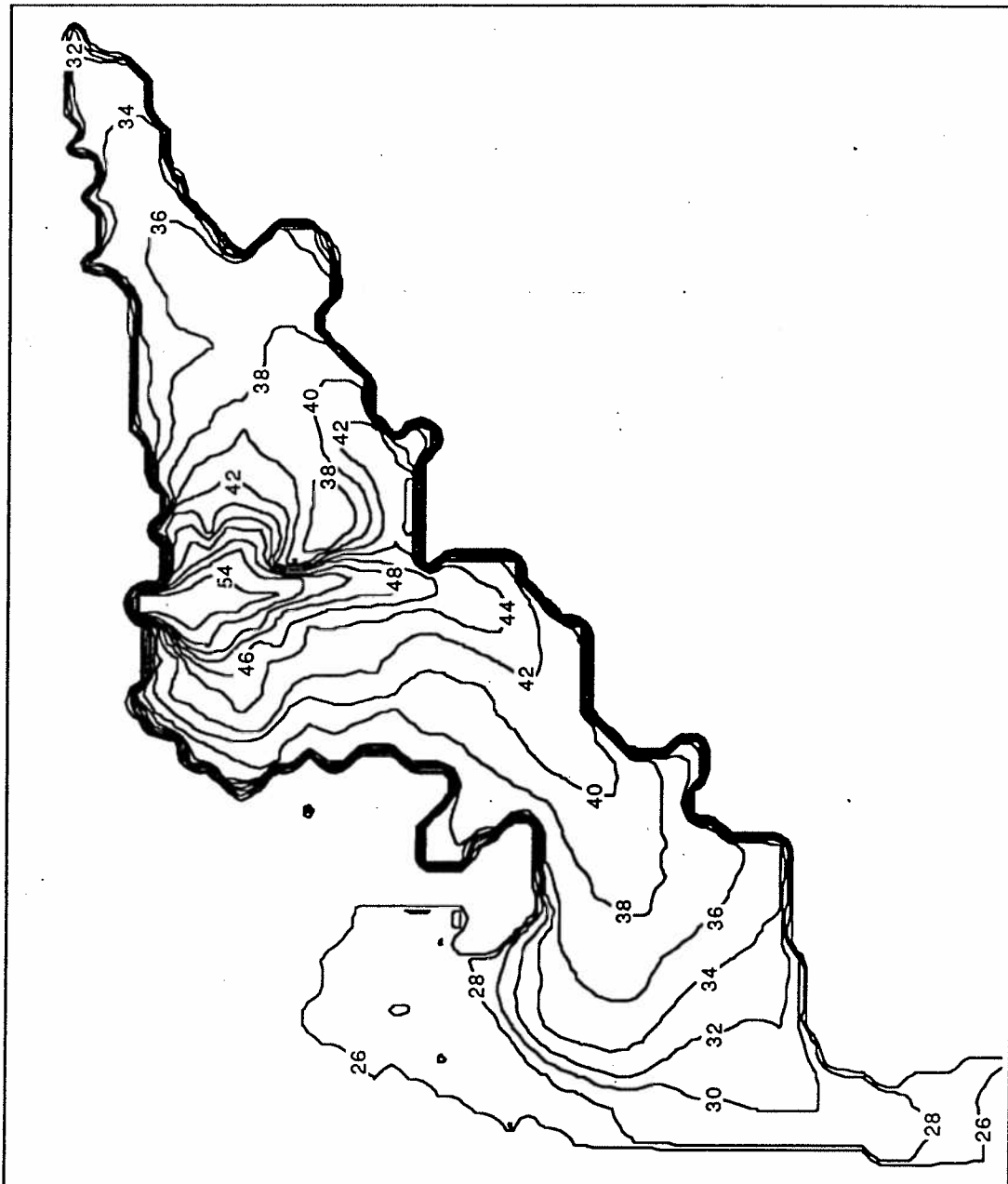


Fig. 5.3.2: Observed temperature ($^{\circ}\text{C}$) distribution in upper part of L Lake on April 25, 1986 at 0936 local time.

UNCLASSIFIED

UNCLASSIFIED

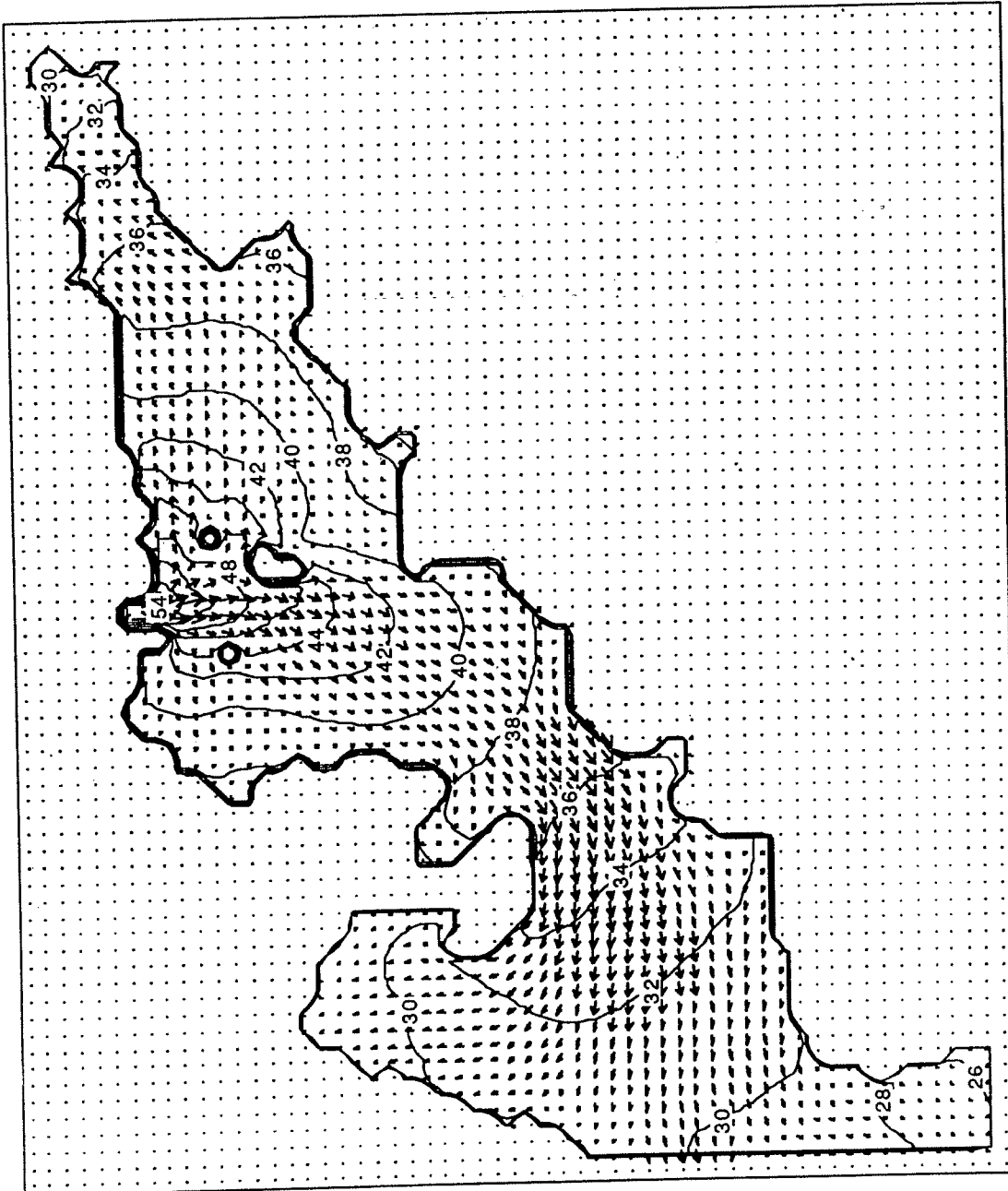


Fig. 5.3.3: Computed temperature contours ($^{\circ}\text{C}$) and flow vectors for upper part of Lake on April 25, 1986 at 1000 local time. Maximum velocity is 0.22 m/s.

UNCLASSIFIED

UNCLASSIFIED

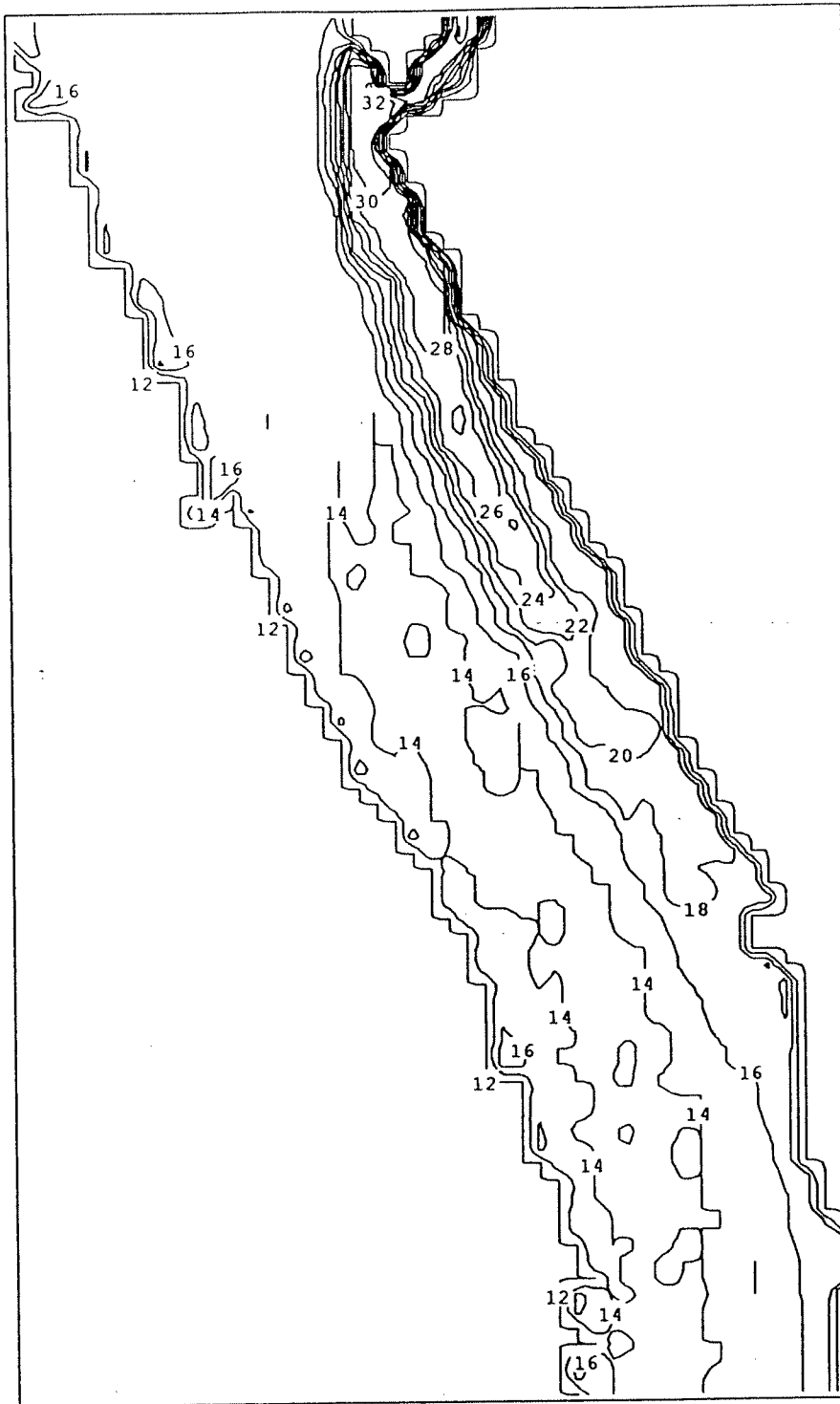


Fig. 5.4.1: Observed temperatures ($^{\circ}\text{C}$) in Savannah River just downstream from mouth of Four Mile Creek on Dec. 4, 1983

UNCLASSIFIED

UNCLASSIFIED

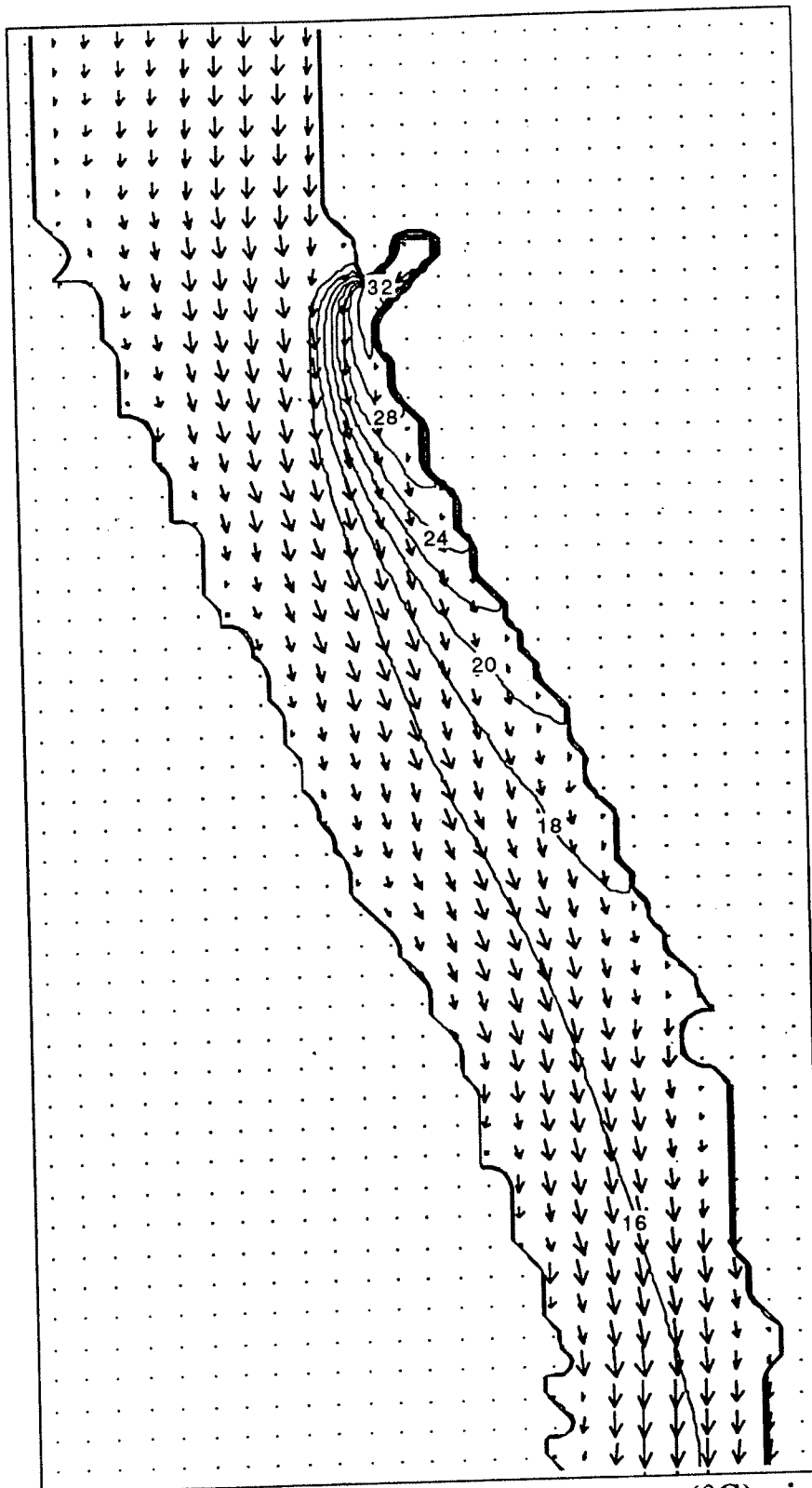


Fig. 5.4.2: Computed temperatures ($^{\circ}\text{C}$) in Savannah River just downstream from mouth of Four Mile Creek on Dec. 4, 1983. Maximum velocity is 0.7 m/s.

UNCLASSIFIED

UNCLASSIFIED

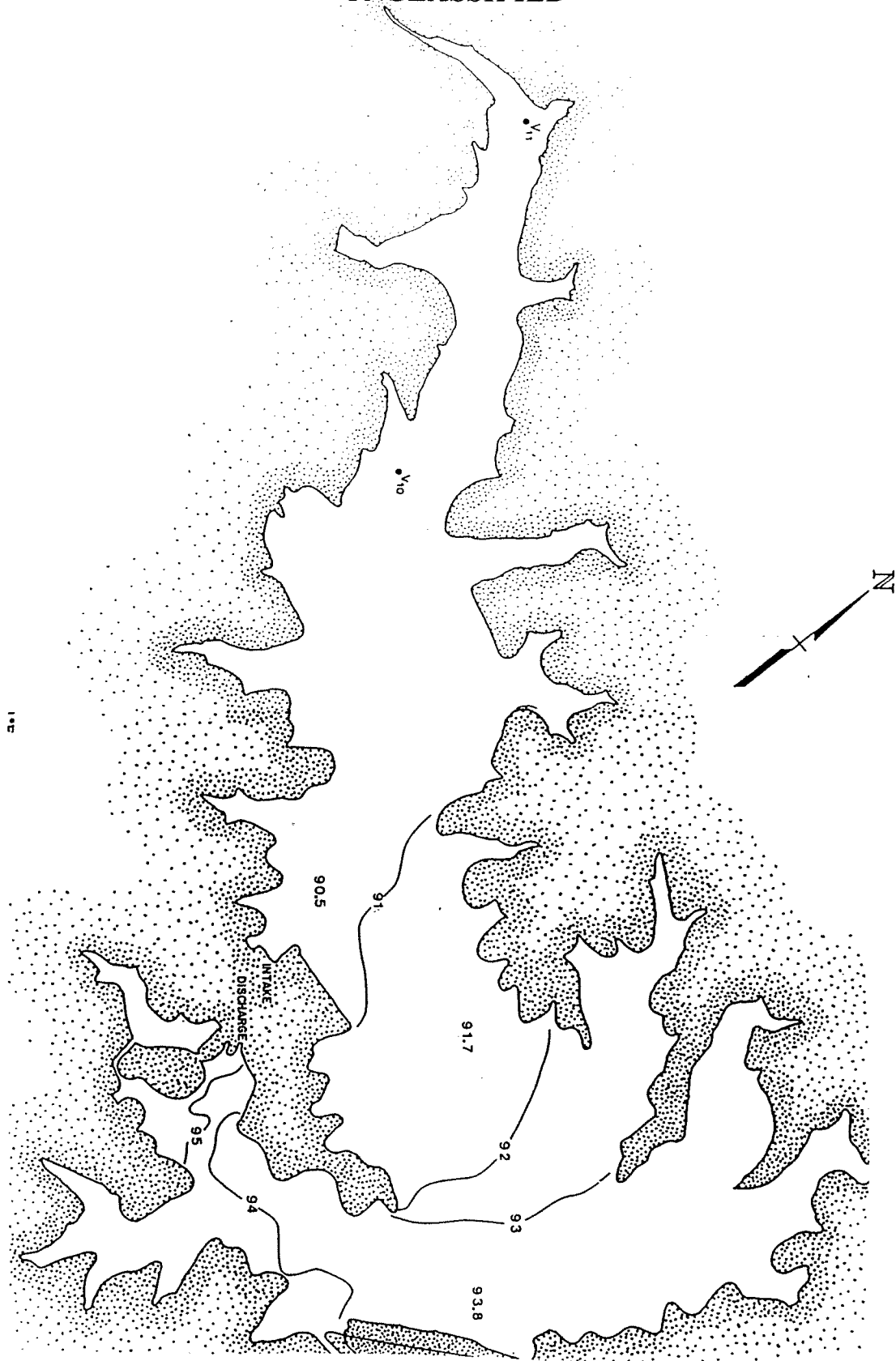


Fig. 5.5.1: Observed temperatures (°F) in Squaw Creek Reservoir on August 17, 1992

UNCLASSIFIED

UNCLASSIFIED

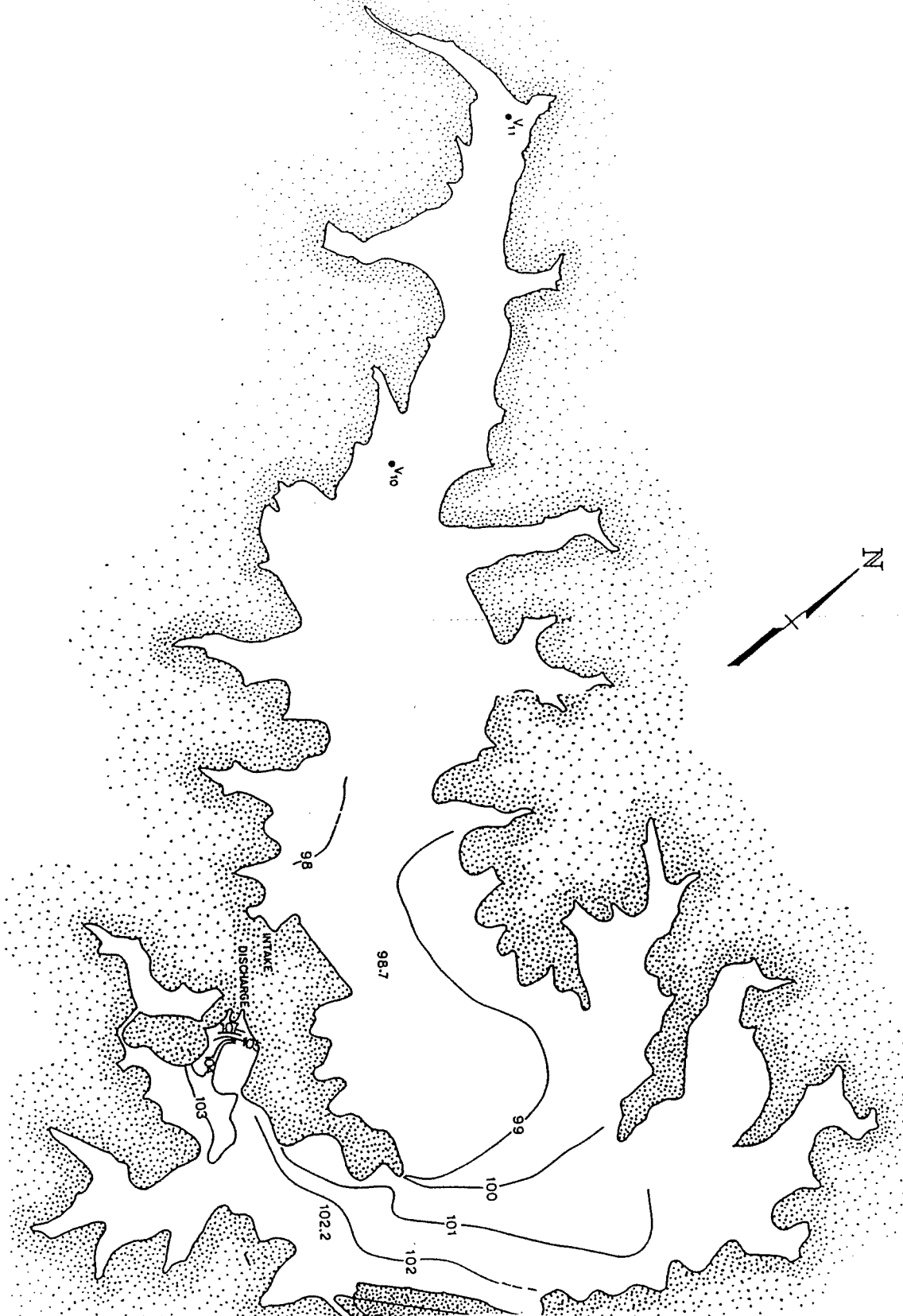


Fig. 5.5.2: Observed temperatures (°F) in Squaw Creek Reservoir on August 11, 1994.

UNCLASSIFIED

UNCLASSIFIED

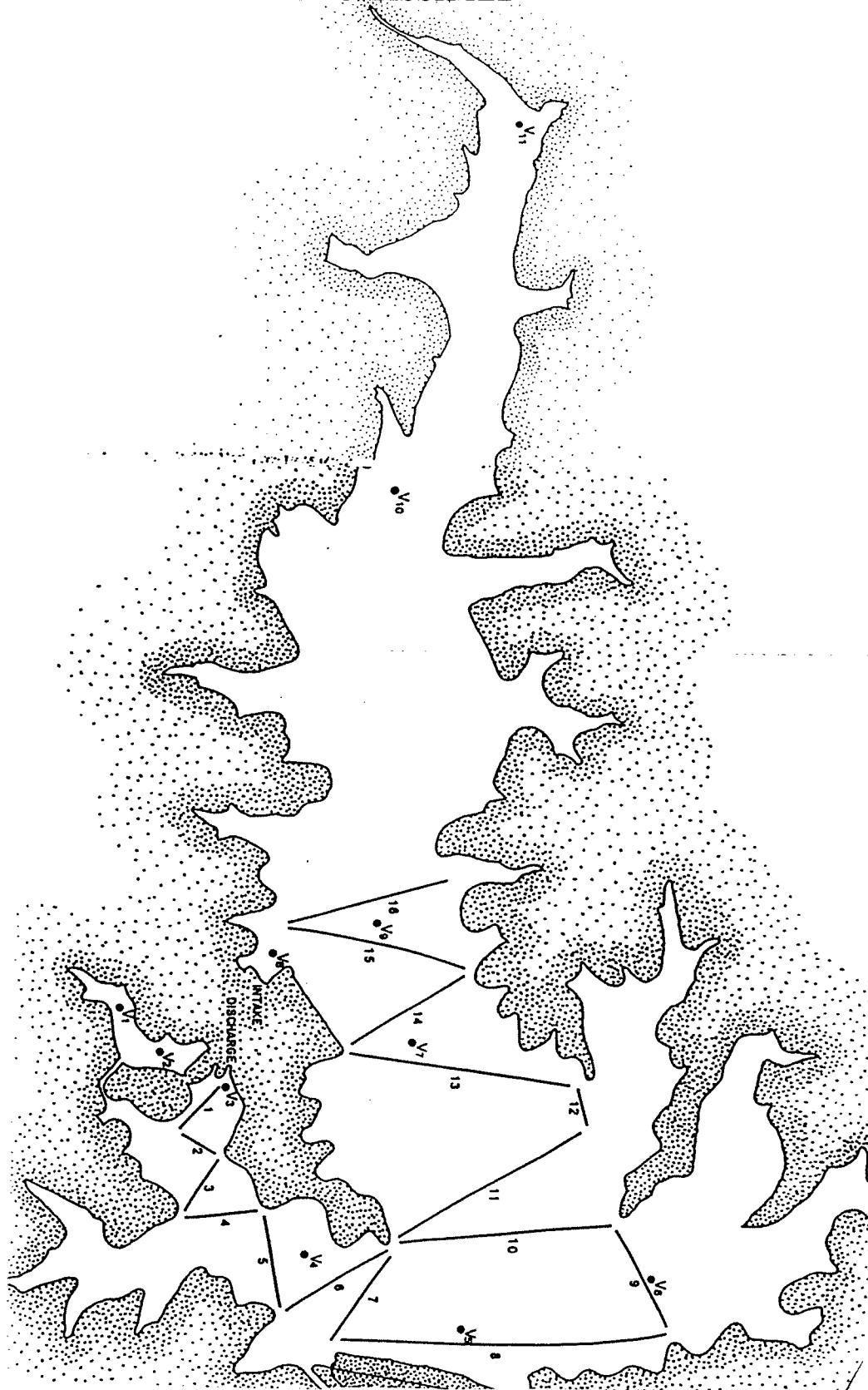


Fig. 5.5.3: Survey tracks and locations of vertical profile stations (V) at Squaw Creek Reservoir.

UNCLASSIFIED

UNCLASSIFIED

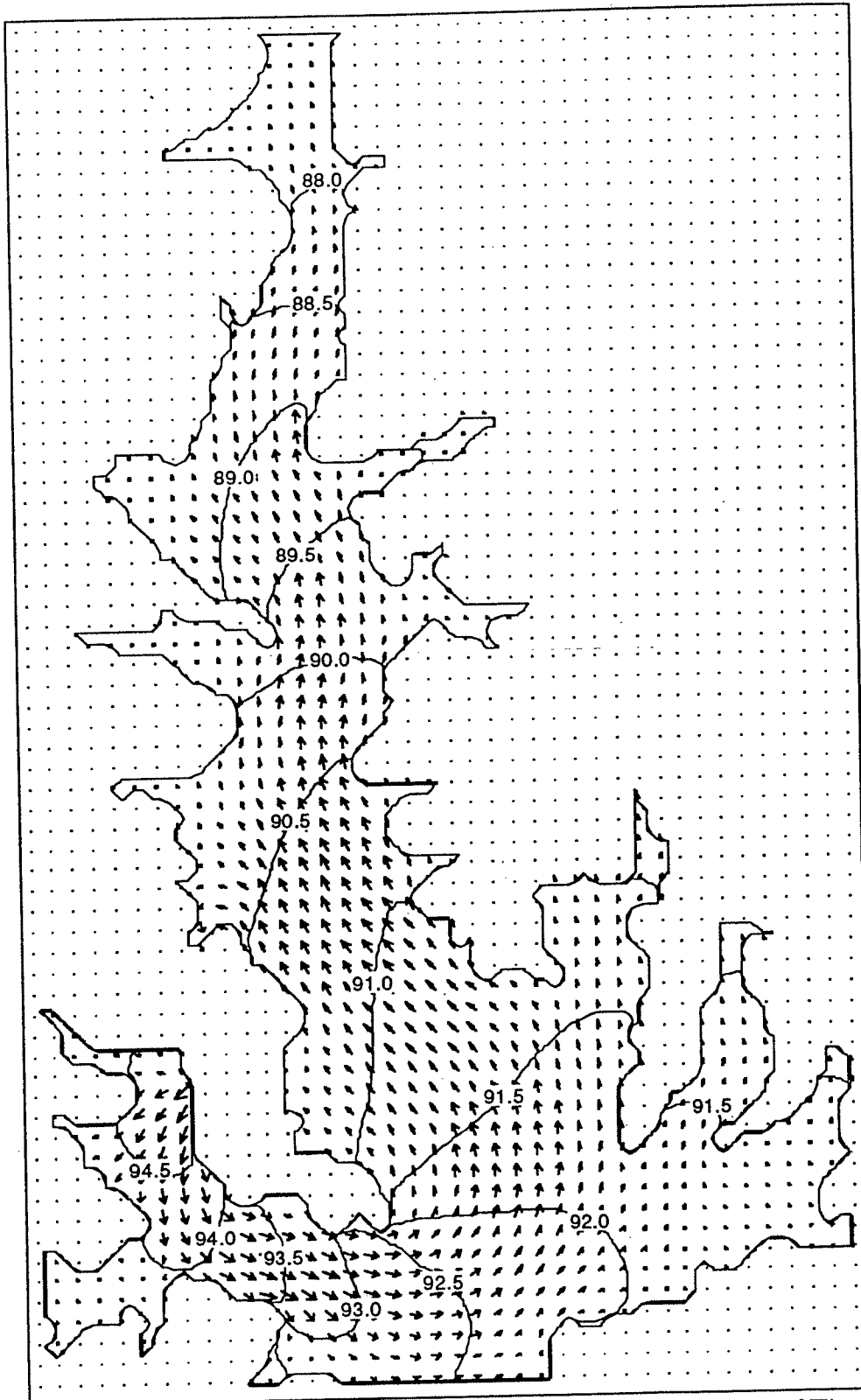


Fig. 5.5.4: Computed temperature contours (°F) and flow vectors for Squaw Creek Reservoir on August 17, 1992. Maximum velocity is 0.29 m/s.

UNCLASSIFIED

UNCLASSIFIED

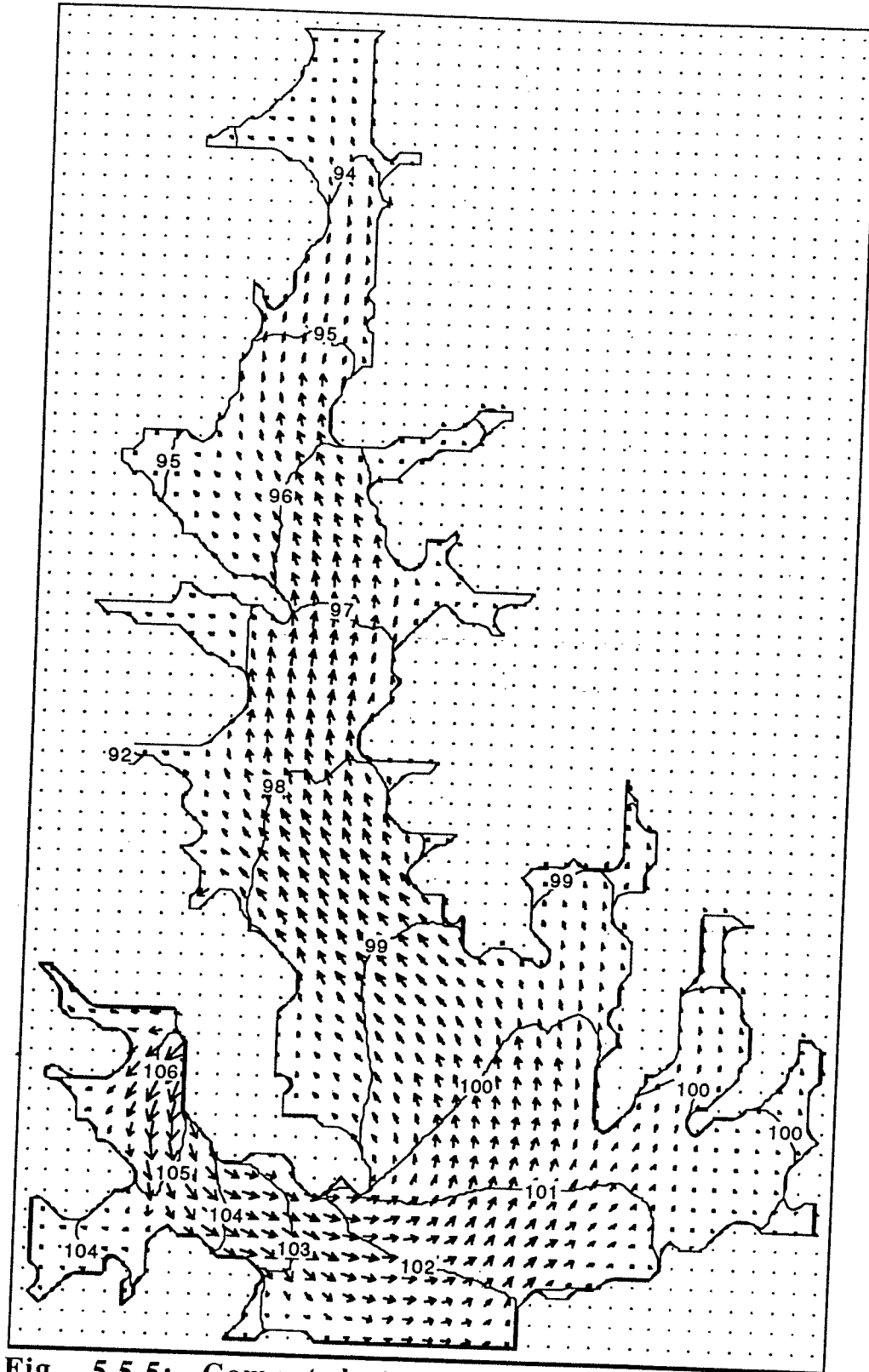


Fig. 5.5.5: Computed temperature contours (°F) and flow vectors for Squaw Creek Reservoir on August 11, 1994. Maximum velocity is 0.24 m/s.

UNCLASSIFIED

